IEEE Open Journal of the
Industrial Electronics Society

Received 20 June 2025; accepted 5 August 2025. Date of publication 7 August 2025;
date of current version 20 August 2025. The review of this article was arranged by Associate Editor Hiralal M. Suryawanshi.

Digital Object Identifier 10.1109/OJIES.2025.3596838

A Design Approach for SoC Integration With Voltage Restoration Capability for Redundancy-Based DC Microgrids

THALES AUGUSTO FAGUNDES [1], RAPHAEL SAUER DE CASTRO [1], MÁRCIO VON RONDOW CAMPOS [1], BRUNO MENEGHEL ZILLI [2], LUCAS JONYS RIBEIRO SILVA [1] (Graduate Student Member, IEEE), JOSEP M. GUERRERO [3] (Fellow, IEEE), AND RICARDO QUADROS MACHADO [1] (Senior Member, IEEE)

[1]Sao Carlos School of Engineering, University of Sao Paulo, Sao Carlos, SP 13566-590, Brazil
[2]University of Technology—Paraná, Guarapuava 85053-525, Brazil
[3]Center for Research on Microgrids (CROM), AAU Energy, Aalborg University, 9220 Aalborg East, Denmark

CORRESPONDING AUTHOR: THALES AUGUSTO FAGUNDES (e-mail: thales.fagundes@usp.br).

This study was supported in part by the Coordination for the Improvement of Higher Education Personnel (CAPES) under Grant PDSE-88881.187771/2018-01, Grant 88881.030370/2013-0, Grant 88887.482911/2020-00, and Grant 88887.182131/2025-00, in part by the National Council for Scientific and Technological Development (CNPq) under Grant 309624/2018-5 and Grant 312664/2021-4, and in part by the Sao Paulo Research Foundation (FAPESP), Brasil under Grant #2013/20721-4, Grant #2020/05865-3, Grant #2022/02721-6, Grant #2022/00628-9, and Grant #2024/00607-7.

ABSTRACT The article presents a secondary voltage control design for an Energy Management System (EMS) in a redundancy-based dc microgrid (MG) through a fuzzy-based approach, suitable for vehicles, aircraft, and medical centers with sensitive loads. Two battery energy storage system (BESS) units serve as common inputs for the redundancy-based dc MG, comprising a cascaded bidirectional Cuk converter (CBC) connected to an auxiliary cascaded bidirectional Boost converter (CBB). The CBC acts as the primary electronic solution, while the CBB enhances reliability by maintaining operation in case of a CBC failure. Furthermore, a Fuel Cell (FC) is linked to the main dc-link of the CBC by a Boost converter. The key contribution lies in the fuzzy-based voltage restoration for the EMS, integrating SoC equalization via S-shaped functions, even during BESS, FC, or CBC maintenance. As the EMS operates as a current source-based system, voltage variations on the dc-link are expected. However, after fuzzy-based restoration, the voltage deviation remains below 2% and the operational efficiency exceeds 90%. Stability analysis is conducted using Lyapunov's indirect method, and the proposed approach is supported by experimental results obtained through SpeedGoat and dSPACE platform interactions.

INDEX TERMS Battery energy storage system (BESS), cascaded bidirectional Boost (CBB), cascaded bidirectional Cuk (CBC), fuzzy-based voltage secondary control, state-of-charge (SoC) equalization.

I. INTRODUCTION

The studies on microgrids (MGs) have been increasing to replace the traditional sources that rely on fossil fuels [1]. In this context, MGs are formed by distributed generation (DG) units, battery energy storage system (BESS) units, and dc loads, coordinated by an energy management system (EMS) [2], [3]. As a result, DG with different characteristics, such as photovoltaic (PV) panels, wind power and fuel cell (FC), can operate with satisfactory performance alongside BESS units. This is because the power generation from PV panels and wind energy sources is intermittent due to environmental factors, while the FC requires a slow transient response that can be compensated by the BESS units [4], [5].

Furthermore, the inclusion of BESS units in MGs requires an EMS to improve efficiency through optimization strategies and SoC equalization. Focusing on SoC balancing, an algorithm to manage the charging/discharging rate of BESS units is crucial to avoid deterioration, and increase their lifetime [6]. Thus, several studies have discussed SoC equalization, such as the application of SoC-based droop, as indicated by [7], [8], [9], [10], while a consensus-based technique is developed by [6]. Additionally, other approaches introduce coordination

among BESS units using fuzzy logic for SoC balancing [2], while the method in [4] employed a sigmoid (S-shaped) function to achieve the same objective.

It is important to note that these methodologies are centered on SoC equalization but do not address voltage restoration at the dc-link, resulting in an inability to regulate it to a predefined reference value.

Considering the approach in [8], a current-source based droop control is proposed to balance the SoC among BESS units in a dc MG. Fortunately, it does not affect power-sharing accuracy, unlike many conventional methods [8]. However, according to [11], while this solution improves accuracy, it also increases voltage deviation on the dc-link, necessitating a secondary control mechanism.

A review in [12] identifies only a few SoC equalization strategies based on a current-source approach, i.e., when the reference from the EMS is directly defined as a current reference, including those in [2], [4], [8], and [13]. In [13], SoC-based droop control was applied to the current loop, with a secondary droop coefficient introduced to reduce control deviations. However, this compensation mechanism is specifically designed for HVDC modular BESS.

In the approach from [8], voltage restoration is incorporated, but the SoC-based droop control sets separate references for charging and discharging currents. This can cause one battery unit to discharge faster than others without charging at the same rate, leading to long-term SoC imbalance and ineffective equalization. Moreover, the methods in [2] and [4] do not consider voltage restoration.

Since an MG is composed of a variety of DGs specified by their intermittency, along with load variation, the dc-link can exhibit voltage deviations [14]. Thus, in the context of a current-source based approach that improves current accuracy, a secondary control embedded within an EMS can mitigate fluctuation events on the dc-ink, ensuring more precise power sharing [15].

Moreover, several approaches address voltage restoration on the dc-link for MGs. For example, in [16], an average voltage and average current PI controller was proposed to improve load current sharing and reconfigure the dc-link voltage. However, this approach does not consider the SoC of the BESS units, which may affect SoC equalization. In [17], a fractional-order compensation droop controller is designed for voltage restoration and also includes BESS units, but it is not applied within an SoC balancing strategy. Similarly, the authors in [18] introduced an additional term in the droop control to include BESS units, but this strategy is also not intended for SoC equalization.

In addition, a dc MG considering redundant modules can improve the configuration because the voltage secondary control is a methodology suitable for sensitive loads, such as electric vehicles, shipboard and aircraft applications [19], [20]. Consequently, the EMS can be improved by through a design of redundancy-based MG.

Integrating a redundancy-based architecture in a MG can be challenging due to the increased complexity associated with additional modules for parameter definition and controller implementation. However, considering the objective of enhancing resilience, it can represent a significant improvement. Moreover, while the inclusion of redundant components inevitably raises costs, it also provides benefits. Ensuring power continuity even in the presence of faults, preventing financial losses and regulatory penalties associated with service interruptions, as some regulations impose fees for electricity outages.

Another significant approach for secondary voltage control, integrated with SoC equalization, involves the use of a fuzzy-based method. This methodology is advantageous because the nonlinearities inherent to the MG do not affect its performance, and its linguistic structure allows for flexible implementation without the need for strict mathematical modeling [21], [22]. Furthermore, in the context of redundancy-based dc MGs, a fuzzy approach is particularly appropriate due to its ability to work independently of the complex system equations [23].

In contrast to the method presented in [24], which requires the EMS to behave as an inverse function—mapping current into a voltage term to adjust the voltage reference—the fuzzy-based control does not rely on such a constraint. The approach in [24] only operates correctly if this inverse functional relationship exists; otherwise, SoC equalization and voltage restoration cannot be properly achieved. The fuzzy-based strategy, on the other hand, does not face this limitation, making it more adaptable to various EMS designs. Lastly, as emphasized in [25], fuzzy logic is also well suited for managing the charging and discharging behavior of BESS units.

Unlike conventional control techniques such as PID, sliding mode control, and model predictive control, the fuzzy-based strategy adopted in this work offers distinct advantages for voltage restoration in redundancy-based DC MGs. First, fuzzy logic control does not require an accurate mathematical model of the system. This feature is particularly beneficial in redundant MG architectures, where nonlinear dynamics, load variability, and converter switching states introduce complex and often unmodeled behaviors.

Moreover, since the proposed approach aims to maintain a constant voltage in a redundancy-based dc MG intended for sensitive loads, it is essential to avoid oscillations. Such oscillations have been observed in PI-based voltage restoration strategies, as reported in [24] and [26]. Among the alternatives, sliding mode control–as proposed in [27]–offers robustness and fast convergence. However, it often introduces chattering effects, which can lead to high-frequency oscillations undesirable for systems supplying sensitive loads. Furthermore, the complexity involved in designing switching surfaces and defining reaching laws presents additional challenges for practical implementation in DC-link voltage restoration.

In the case of model predictive control-based approaches, such as those presented in [28], [29], the advantage lies in predictive performance and the ability to manage multiple constraints. Nevertheless, the requirement for high

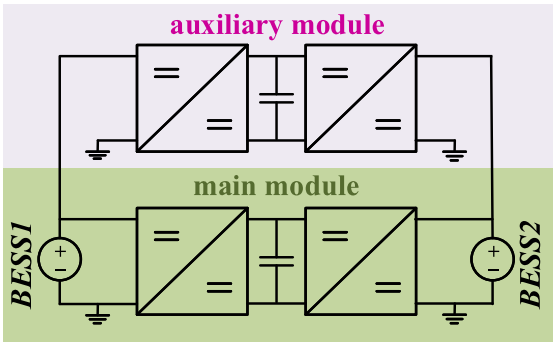

FIGURE 1. Proposed redundancy-based DC MG.

computational power and accurate real-time models limits the feasibility of model predictive control for embedded EMS platforms in MGs. In addition, these strategies do not always focus on voltage restoration, and may introduce substantial current oscillations, as indicated in [28], [29], which can be harmful for FC and sensitive loads. In contrast, the proposed fuzzy-based secondary voltage control directly integrates the voltage deviation into its rule base, enabling flexible and real-time adjustment of the voltage reference using a current source-based logic.

Thus, this article introduces a fuzzy-based secondary voltage control tailored for BESS units, combined with an SoC-sharing technique to maintain SoC equalization and enhance the EMS through S-shaped functions, which are designed based on a current-source approach. The proposed method is designed for a redundancy-based dc MG (see Fig. 1) that comprises a cascaded bidirectional Cuk converter (CBC) and a cascaded bidirectional Boost converter (CBB). Both converters share the BESS units at their inputs, with the CBC functioning as the main module and the CBB as a backup module, to guarantee continuous EMS operation during CBC failure or maintenance.

Furthermore, a FC is linked to the main dc-link through a Boost converter and operates with a droop controller designed to reduce membrane stress caused by dc load fluctuations. Thus, the BESS units are responsible to absorb the transient from the main dc-link. Regarding the secondary voltage control strategy, a fuzzy-based solution embedded in the EMS, aims to maintain a specific voltage level during unpredictable events in the redundancy-based dc MG and facilitates SoC equalization. To analyze stability, the authors modify the proposed technique presented in [30] and employ Lyapunov's indirect method to account for the interaction among the CBC, CBB, and FC converter operating with the EMS, ensuring the dc-link works at a specific level.

Therefore, the main contributions of this article are listed as follows.

1) A fuzzy-based secondary voltage control operating alongside SoC equalization, designed as a current-source-based strategy to improve accuracy.
2) An alternative technique for improving S-shaped functions through voltage restoration.
3) The EMS for the BESS units can compensate load variations in conjunction with secondary voltage control.
4) Even in the event of a failure or maintenance in the CBC, the power flow can be redirected through the CBB.
5) Although a low-bandwidth communication is necessary for voltage restoration, EMS operation occurs in a decentralized manner.

The rest of this article is organized as follows. Section II introduces the redundancy-based DC-DC converter, while Section III presents the redundancy-based DC MG. The proposed secondary voltage control is examined in Section IV. Efficiency analysis is evaluated in Section V, while stability analysis is demonstrated in Section VI. Subsequently, Section VII presents experimental results through hardware-in-the-loop (HIL). Finally, Section VIII concludes this article.

II. REDUNDANCY-BASED DC–DC CONVERTER

In Fig. 2, CBC and CBB share two common inputs, connecting BESS1 and BESS2 to the main DC-link (where the local loads are installed). Thus, BESS1 has the terminal voltage v_{bat1} and current i_{bat1}, while the terminal voltage of BESS2 is v_{bat2} with a corresponding current labeled as i_{bat2}. Considering BESS1, i_{bat1} is divided into i_{L1} and i_{L5} through the inductances L_1 and L_5. In addition, the current i_{bat2} flows through the CBC across the inductance L_3 (with a current i_{L3}) and through the CBB via the inductance L_6 (with a current i_{L6}).

Concerning the controlled semiconductors in the redundancy-based topology, S_1 and S_2 receive the PWM signals in the CBC (k_1 and k_2), while S_3 and S_4 are controlled by the PWM signals in the CBB (k_3 and k_4). Subsequently, $\bar{S}_1$, $\bar{S}_2$, $\bar{S}_3$, and $\bar{S}_4$ receive the complementary signals. In the CBC, the capacitor C_1 (with a voltage v_{C1}) absorbs energy from BESS1, while C_2 (with a voltage v_{C2}) absorbs energy from BESS2.

In addition, the inductances L_2 and L_4 generate continuous currents i_{L2} and i_{L4}. In this context, Cuk1 and Cuk2 from the CBB are connected through the main dc-link (C_o) with voltage v_o, supplying the linear load R_o. Two bidirectional Cuk converters (Cuk1 and Cuk2) connected to the main dc-link (via the capacitor C_o) constitute the CBC, while two bidirectional Boost converters connected to the capacitor C_3 form the CBB.

In Fig. 2, the inductance losses are denoted by r_{L1}, r_{L2}, r_{L3}, r_{L4}, r_{L5}, and r_{L6}. In addition, capacitance losses are categorized as r_{C1}, r_{C2}, r_{C3}, and r_{Co}, while the internal resistances of the BESS units are denoted by r_{bat1} and r_{bat2}.

A. ELEMENTS SELECTION OF THE REDUNDANCY-BASED DC–DC CONVERTER

The model of the redundancy-based dc–dc converter shown in Fig. 2 is obtained from [31]. Based on the matrices $\boldsymbol{A}$, $\boldsymbol{B}$, $\boldsymbol{C}$, and $\boldsymbol{D}$, the following explanation outlines how the inductances (L_1, L_2, L_3, L_4, L_5, and L_6) and capacitances (C_1, C_2, C_3, and C_o) were determined.

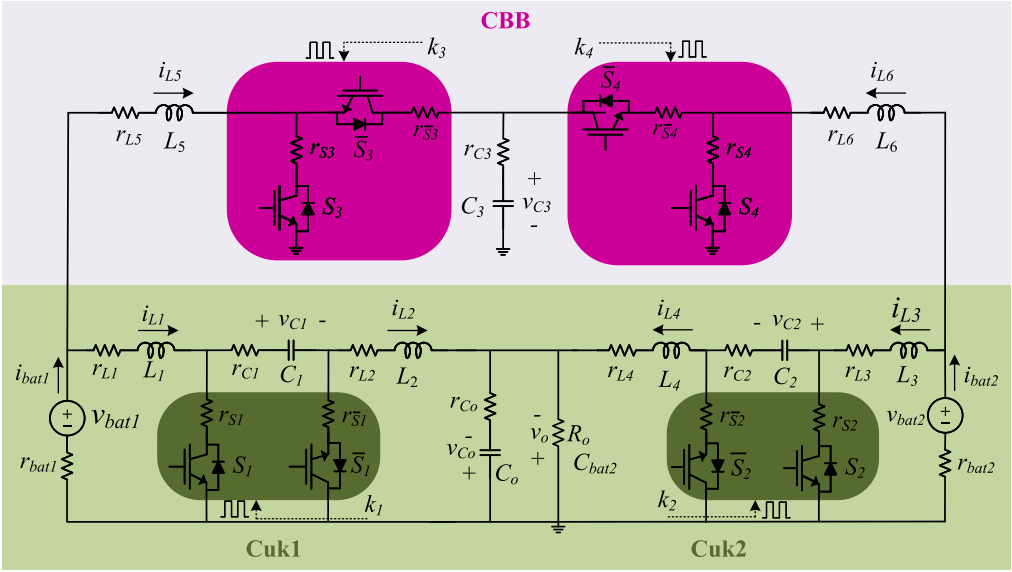

FIGURE 2. Redundancy-based dc–dc converter from [31].

Therefore, in (1) shown at the bottom of the next page, is defined the complete state-space model $\boldsymbol{A}$ (with $A_{1,1}$, $A_{2,2}$, $A_{4,4}$, $A_{5,5}$, $A_{7,7}$, and $A_{8,8}$ presented in (2)), shown at the bottom of the next page, the input matrix $\boldsymbol{B}$ is given in (3), and the output matrices $\boldsymbol{C}$ and $\boldsymbol{D}$ are determined in (4) and (5), respectively.

$$\boldsymbol{B} = \begin{bmatrix} \frac{1}{L_1} & 0 \\ 0 & 0 \\ 0 & 0 \\ 0 & \frac{1}{L_3} \\ 0 & 0 \\ 0 & 0 \\ \frac{1}{L_5} & 0 \\ 0 & \frac{1}{L_6} \\ 0 & 0 \\ 0 & 0 \end{bmatrix} \tag{3}$$

$$\boldsymbol{C} = \begin{bmatrix} 1 & 0 & 0 & 0 & 0 & 0 & 0 & 0 & 0 & 0 \\ 0 & 0 & 0 & 1 & 0 & 0 & 0 & 0 & 0 & 0 \\ 0 & 0 & 0 & 0 & 0 & 0 & 1 & 0 & 0 & 0 \\ 0 & 0 & 0 & 0 & 0 & 0 & 0 & 1 & 0 & 0 \\ 0 & \frac{R_o r_{Co}}{R_o + r_{Co}} & 0 & 0 & \frac{R_o r_{Co}}{R_o + r_{Co}} & 0 & 0 & 0 & 0 & \frac{R_o r_{Co}}{R_o + r_{Co}} \end{bmatrix} \tag{4}$$

$$\boldsymbol{D} = \begin{bmatrix} 0 & 0 \\ 0 & 0 \\ 0 & 0 \\ 0 & 0 \\ 0 & 0 \end{bmatrix}. \tag{5}$$

Considering four PWM signals used to drive the active semiconductors, a total of 16 sub-circuits can be formed, based on the 2^n combinations (where $n = 4$). Table 1 presents the status of each semiconductor–marked with ✓ when closed and χ when open–corresponding to these 16 possible configurations.

In the operation of the redundancy-based dc–dc converter, with all duty cycles between 0 and 1, there are at least two active subcircuits ($k_1 = k_2 = k_3 = k_4$) and a maximum of five active sub-circuits ($k_1 \neq k_2 \neq k_3 \neq k_4$). Adopting the redundancy-based dc–dc converter composed of components with no internal losses, the steady-state average value of the state vector is defined as follows:

$$\begin{cases} I_{L1} = \frac{\gamma}{\alpha\beta+\gamma}(I_1 - \alpha I_2 + \alpha\beta\frac{V_o}{R_o}) \\ I_{L2} = \frac{1}{\alpha\beta+\gamma}(I_1 - \alpha I_2 + \alpha\beta\frac{V_o}{R_o}) \\ I_{L3} = -\frac{\beta}{\alpha\beta+\gamma}(I_1 - \alpha I_2 - \gamma\frac{V_o}{R_o}) \\ I_{L4} = -\frac{1}{\alpha\beta+\gamma}(I_1 - \alpha I_2 - \gamma\frac{V_o}{R_o}) \\ I_{L5} = \frac{\alpha}{\alpha\beta+\gamma}(\beta I_1 + \gamma I_2 - \beta\gamma\frac{V_o}{R_o}) \\ I_{L6} = \frac{1}{\alpha\beta+\gamma}(\beta I_1 + \gamma I_2 - \beta\gamma\frac{V_o}{R_o}) \\ V_{C1} = \frac{V_1}{1-k_1} \\ V_{C2} = \frac{V_2}{1-k_2} \\ V_{C3} = \frac{V_1}{1-k_3} = \frac{V_2}{1-k_4} \\ V_{Co} = -\frac{V_1 k_1}{2-(k_1+k_2)} - \frac{V_2 k_2}{2-(k_1+k_2)} \end{cases} \tag{6}$$

where $\alpha = -(\frac{1-k_4}{1-k_3})$, $\beta = -(\frac{k_2}{1-k_2})$ e $\gamma = -(\frac{k_1}{1-k_1})$.

Furthermore, in Figs. 3 and 4, an initial simulation in PSIM was conducted to demonstrate the steady-state behavior of each component without considering parasitic losses, where T_s represents the switching period. It is observed that Δi_{L1},

TABLE 1. Subcircuit States of the Redundancy-Based DC-DC Converter

Subcircuit	S_1	S_2	S_3	S_4	Closed Semiconductors
1	✓	✓	✓	✓	4
2	✓	✓	✓	χ	3
3	✓	✓	χ	✓	3
4	✓	χ	✓	✓	3
5	χ	✓	✓	✓	3
6	✓	✓	χ	χ	2
7	✓	χ	✓	χ	2
8	✓	χ	χ	✓	2
9	χ	✓	✓	χ	2
10	χ	✓	χ	✓	2
11	χ	χ	✓	✓	2
12	✓	χ	χ	χ	1
13	χ	✓	χ	χ	1
14	χ	χ	✓	χ	1
15	χ	χ	χ	✓	1
16	χ	χ	χ	χ	0

Δi_{L2}, and Δv_{C1} are influenced by k_1, while Δi_{L3}, Δi_{L4}, and Δv_{C1} are influenced by k_2. In addition, Δi_{L5} is related to k_3, and Δi_{L6} is related to k_4, while k_3 and k_4 determine the behavior of Δv_{C3}. Finally, $v_{Co} < 0$ represents the output of a conventional Cuk converter, remaining constant throughout all switching intervals, thus adopting $\Delta v_{Co} \approx 0$.

Considering the influence of each duty cycle associated with the redundancy-based DC-DC converter structure: k_1 for the Cuk1, k_2 for the Cuk2, and k_3 and k_4 for the CBB, the current ripple for the inductances and the voltage ripple across the capacitances are defined in (7), where I_{L2}, I_{L4}, I_{L5}, and I_{L6} are given in (6).

$$\begin{cases} \Delta i_{L1} = \frac{k_1 V_{bat1}}{2L_1 f_s} \\ \Delta i_{L2} = \frac{k_1 V_{bat1}}{2L_2 f_s} \\ \Delta i_{L3} = \frac{k_2 V_{bat2}}{2L_3 f_s} \\ \Delta i_{L4} = \frac{k_2 V_{bat2}}{2L_4 f_s} \\ \Delta i_{L5} = \frac{k_3 V_{bat1}}{2L_5 f_s} \\ \Delta i_{L6} = \frac{k_4 V_{bat2}}{2L_6 f_s} \\ \Delta v_{C1} = \frac{|I_{L2}|k_1}{2C_1 f_s} \\ \Delta v_{C2} = \frac{|I_{L4}|k_2}{2C_2 f_s} \\ \Delta v_{C3} \approx 0 \\ \Delta v_{Co} \approx 0. \end{cases} \tag{7}$$

Furthermore, adopting $V_{bat1} = 42.2\,\text{V}$, $V_{bat2} = 17.95\,\text{V}$, $k_1 = 0.347$, $k_2 = 0.478$, $k_3 = 0.280$, $k_4 = 0.665$, $R_o = 24\,\Omega$,

$$\boldsymbol{A} = \begin{bmatrix} A_{1,1} & \frac{k_1 r_{S1} + r_{\bar{S}1}(1-k_1)}{L_1} & -\frac{1-k_1}{L_1} & 0 & 0 & 0 & -\frac{r_{bat1}}{L_1} & 0 & 0 & 0 \\ \frac{k_1 r_{S1} + r_{\bar{S}1}(1-k_1)}{L_2} & A_{2,2} & -\frac{k_1}{L_2} & 0 & -\frac{R_o r_{Co}}{L_2(R_o+r_{Co})} & 0 & 0 & 0 & 0 & -\frac{R_o}{L_2(R_o+rco)} \\ \frac{1-k_1}{C_1} & \frac{k_1}{C_1} & 0 & 0 & 0 & 0 & 0 & 0 & 0 & 0 \\ 0 & 0 & 0 & A_{4,4} & \frac{k_2 r_{S2} + r_{\bar{S}2}(1-k_2)}{L_3} & -\frac{1-k_2}{L_3} & 0 & -\frac{r_{bat2}}{L_3} & 0 & 0 \\ 0 & -\frac{R_o r_{Co}}{L_4(R_o+r_{Co})} & 0 & \frac{k_2 r_{S2} + r_{\bar{S}2}(1-k_2)}{L_4} & A_{5,5} & -\frac{k_2}{L_4} & 0 & 0 & 0 & -\frac{R_o}{L_4(R_o+r_{Co})} \\ 0 & 0 & 0 & \frac{1-k_2}{C_2} & \frac{k_2}{C_2} & 0 & 0 & 0 & 0 & 0 \\ -\frac{r_{bat1}}{L_5} & 0 & 0 & 0 & 0 & 0 & A_{7,7} & \frac{r_{C3}(k_3+k_4+|k_3-k_4|-2)}{2L_5} & -\frac{1-k_3}{L_5} & 0 \\ 0 & 0 & 0 & -\frac{r_{bat2}}{L_6} & 0 & 0 & \frac{r_{C3}(k_3+k_4+|k_3-k_4|-2)}{2L_6} & A_{8,8} & -\frac{1-k_4}{L_6} & 0 \\ 0 & 0 & 0 & 0 & 0 & 0 & \frac{1-k_3}{C_3} & \frac{1-k_4}{C_3} & 0 & 0 \\ 0 & \frac{R_o}{C_o(R_o+r_{Co})} & 0 & 0 & \frac{R_o}{C_o(R_o+r_{Co})} & 0 & 0 & 0 & 0 & -\frac{1}{C_o(R_o+r_{Co})} \end{bmatrix} \tag{1}$$

$$A_{1,1} = -\frac{(1-k_1)(r_{bat1} + r_{C1} + r_{L1} + r_{\bar{S}1}) + k_1(r_{bat1} + r_{L1} + r_{S1})}{L_1}$$

$$A_{2,2} = -\frac{(1-k_1)}{L_2}\left(r_{L2} + r_{\bar{S}1} + \frac{R_o r_{Co}}{R_o + r_{Co}}\right) - \frac{k_1}{L_2}\left(r_{C1} + r_{L2} + r_{S1} + \frac{R_o r_{Co}}{R_o + r_{Co}}\right)$$

$$A_{4,4} = -\frac{(1-k_2)(r_{bat2} + r_{C2} + r_{L3} + r_{\bar{S}2}) + k_2(r_{bat2} + r_{L3} + r_{S2})}{L_3}$$

$$A_{5,5} = -\frac{(1-k_2)}{L_4}\left(r_{L4} + r_{\bar{S}2} + \frac{R_o r_{Co}}{R_o + r_{Co}}\right) - \frac{k_2}{L_4}\left(r_{C2} + r_{L4} + r_{S2} + \frac{R_o r_{Co}}{R_o + r_{Co}}\right)$$

$$A_{7,7} = -\frac{r_{bat1} + r_{C3} + r_{L5} + r_{\bar{S}3} - k_3 r_{C3} + k_3 r_{S3} - k_3 r_{\bar{S}3}}{L_5}$$

$$A_{8,8} = -\frac{r_{bat2} + r_{C3} + r_{L6} + r_{\bar{S}4} - k_4 r_{C3} + k_4 r_{S4} - k_4 r_{\bar{S}4}}{L_6}. \tag{2}$$

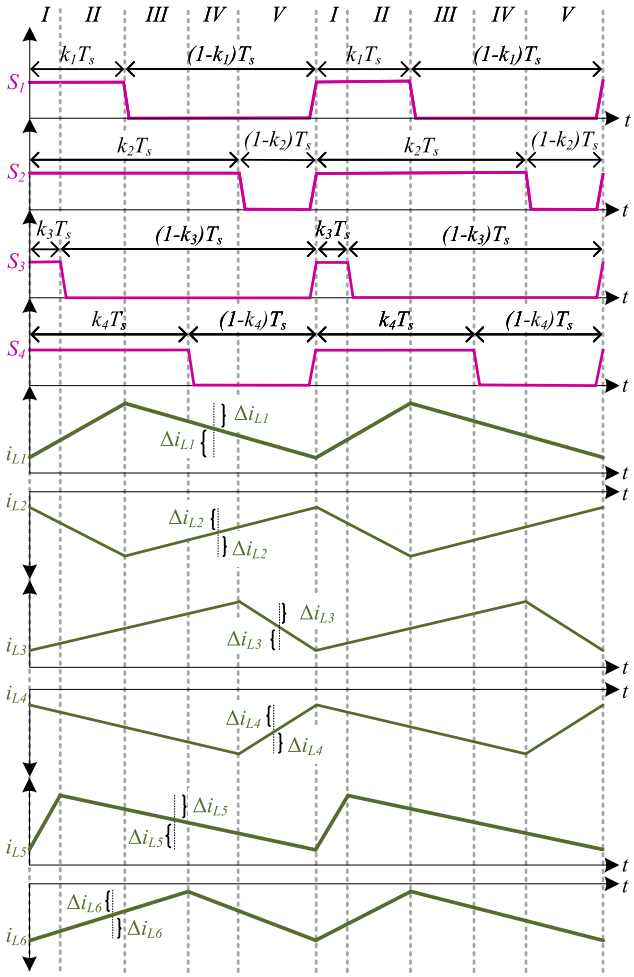

FIGURE 3. Expected inductor currents in the simulation without internal component losses.

TABLE 2. Parameters Value

Component	*Value*	*Ripple (%)*
L_1	4,8 mH	3,61
L_2	4,8 mH	2,05
L_3	4,8 mH	1,54
L_4	4,8 mH	1,48
L_5	4,8 mH	5,05
L_6	4,8 mH	2,71
C_1	130 μF	1,8
C_2	130 μF	3,8
C_3	470 μF	≈ 0
C_o	470 μF	≈ 0

and the switching frequency of 10 kHz in (6) and (7), the components are defined according to the maximum ripple (%) for each voltage and current. The results are presented in Table 2, with parasitic losses considered in Table 3.

B. COST ANALYSIS OF THE REDUNDANCY-BASED DC–DC CONVERTER

Table 4 presents a comparative summary of selected dc–dc converter topologies (see Fig. 2) based on their key characteristics, including bidirectionality, fault tolerance through

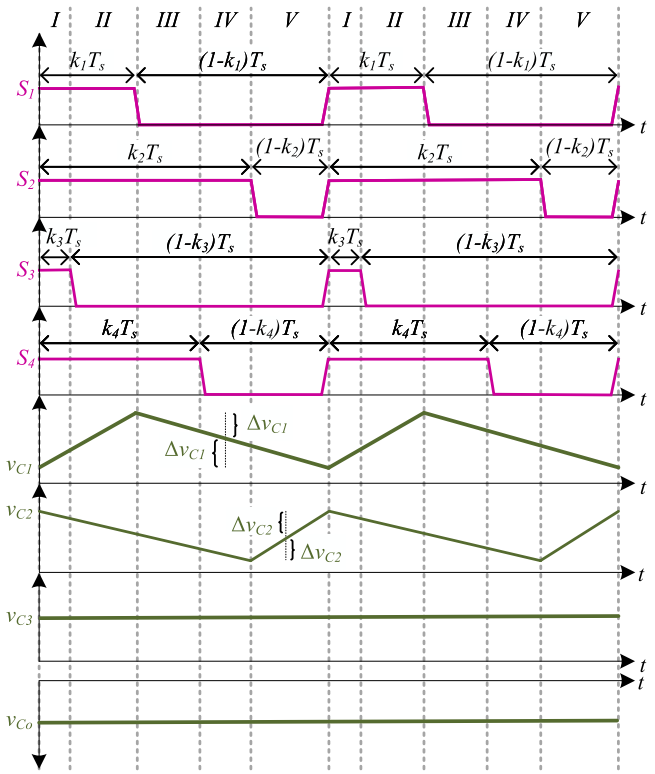

FIGURE 4. Expected capacitor voltages in the simulation without internal component losses.

TABLE 3. Parasitic Losses From the Redundancy-Based DC–DC Converter

Parameter	*Value* ($m\Omega$)
$r_{L1} = r_{L2} = r_{L3} = r_{L4} = r_{L5} = r_{L6}$	150
$r_{bat1} = r_{bat2}$	10
$r_{C1} = r_{C2}$	30
$r_{S1} = r_{S2} = r_{S3} = r_{S4}$	30
$r_{\bar{S}1} = r_{\bar{S}2} = r_{\bar{S}3} = r_{\bar{S}4}$	30
$r_{Co} = r_{C3}$	150

redundancy, the presence of high-frequency transformers, control complexity, and estimated cost (USD/kW). The redundancy criterion considers whether the converter includes reconfigurable paths or redundant modules to maintain power flow under fault conditions.

Control complexity is qualitatively classified as moderate or high, according to the number of control loops, the type of feedback (centralized versus distributed), the need for intermodular synchronization, and the nature of switching strategies (e.g., PWM versus soft switching with zero-voltage or zero-current transitions). Cost estimations are derived from a per-kilowatt projection using common market values for key components, including power switches, passive elements, and control circuitry. The redundancy-based topology stands out by offering bidirectional operation and embedded redundancy with a moderate control structure and competitive implementation cost, which is favorable when compared to other advanced topologies that require higher coordination effort and additional hardware resources.

TABLE 4. Comparison of Converter Topologies: Technical Characteristics and Estimated Cost

Attribute	Proposed Work	[32]	[33]	[34]
Topology	Cuk + Boost Redundant	Soft-Switching with Fault Bypass	Modular Multilevel Converter	Three-Phase Multilevel with Floating Capacitors
Bidirectional	Yes	Yes	Yes	No
Redundancy	Yes (CBC and CBB)	Yes (module bypass)	Yes (submodule level)	Yes (reconfigurable multilevel phases)
Transformers	No	Yes (3 high-frequency)	No	No
Control Complexity	Moderate	High	High	High
Estimated Cost (USD/kW)	84.00	119.00	144.00	69.60

Among the reviewed topologies in Table 4, the architecture proposed by [34] presents a lower estimated cost. However, it is not bidirectional, and the converter includes fault-tolerant behavior through phase-level reconfiguration, which can be considered a form of redundancy in a modular multilevel context. In addition, its control is more complex due to the use of floating capacitors and the need for balancing mechanisms across phases. Compared to the redundancy-based dc–dc converter in this approach, which provides a simpler control and native bidirectional power flow, the solution from [34] requires more implementation effort even with its cost advantage.

In contrast, the other analyzed references, from [32] and [33], involve soft-switching and modular multilevel architectures that, while bidirectional and redundant, rely on high-frequency transformers and advanced intermodular control strategies. These features significantly increase the complexity of implementation and hardware requirements, resulting in higher estimated costs (USD/kW). Therefore, the topology is this approach achieves a balanced tradeoff between cost, redundancy, and control simplicity, making it more suitable for scalable and reliable dc MG applications.

III. CONFIGURATION OF THE REDUNDANCY-BASED DC MG

From Fig. 2, the redundancy-based dc MG is formed, as illustrated in Fig. 5. In this context, Cuk1 and Cuk2 from the CBB are connected through C_{bat1} (with voltage v_{obat1}) and C_{bat2} (with voltage v_{obat2}), along with the line resistances r_{line_bat1} and r_{line_bat2}, while the main dc-link voltage is v_o, supplying the linear load R_o.

In addition, the FC is connected to the main dc-link by a Boost converter via the line resistance r_{line_fc}, as shown in Fig. 5. In this diagram, the FC current i_{fc} $(= i_{Lfc})$ flows through the inductance L_{fc}, while the active switch S_{fc} receives the PWM signal k_{fc} and D_{fc} is identified as a diode. Similarly, the output capacitance of the Boost converter is defined as C_{fc}, with an associated voltage v_{ofc}.

In Fig. 5, regarding the losses from the redundancy-based dc–dc converter listed previously, the inductance loss from the Boost is denoted as r_{Lfc}, while the diode loss is represented by r_{Dfc}. Additionally, the capacitance losses are denoted as r_{Cb1}, r_{Cb2}, r_{Cfc}, and r_{Co}.

The approach proposed in [20] develops a redundancy-based dc MG for SoC equalization using the CBB and CBC modules; however, it does not incorporate voltage restoration. In contrast, this article adopts a different strategy: the CBB operates as the main module, while the CBC functions as a backup to ensure resilience by redirecting power flow during uncertain events–such as failures or maintenance–in the CBB converters, including disruptions in the operation of Cuk1 or Cuk2. In addition, as described in [35], the Cuk topology is suitable for loads requiring minimal stress and exhibiting small current ripple, making it ideal for secondary voltage control within an EMS.

In addition, the redundancy-based dc MG is well suited to support SoC equalization among BESS units, as the topologies in [32], [33], and [34] do not include redundant modules capable of maintaining a constant dc-link voltage during faults. Furthermore, the configurations in [32] and [34] are not designed to accommodate BESS units for SoC equalization. Therefore, although the inclusion of additional modules increases system cost, the redundancy-based dc MG offers a reliable mechanism for applications that require continuous power delivery.

Although a conventional dc MG (i.e., dc–dc converters connected to a common dc-link) could perform SoC equalization among BESS units, power flow redirection in the event of a failure in the main CBC is only feasible in the redundancy-based dc MG. Moreover, unlike [36], the redundancy-based dc MG has two input ports, each receiving a BESS unit, whereas [36] lacks an auxiliary mechanism to redirect power flow and is instead designed to supply two output loads. Consequently, [36] cannot achieve the same level of performance as the redundancy-based dc MG.

IV. DESIGN OF THE SECONDARY VOLTAGE CONTROL FOR THE EMS

Briefly, the EMS is introduced, which is important for the coordination among the sources, as represented in Fig. 6. It is important to highlight that the method for determining the proportional-integral (PI) controller parameters of the redundancy-based topology was presented in [31]. Therefore, with regard to the FC, the droop controller with a delay in the load response to prevent damage to the FC membranes is presented, followed by its secondary voltage control. Later, the SoC-sharing strategy is introduced with a rapid response to compensate load transients, followed by the fuzzy-based secondary control in the EMS from the BESS units.

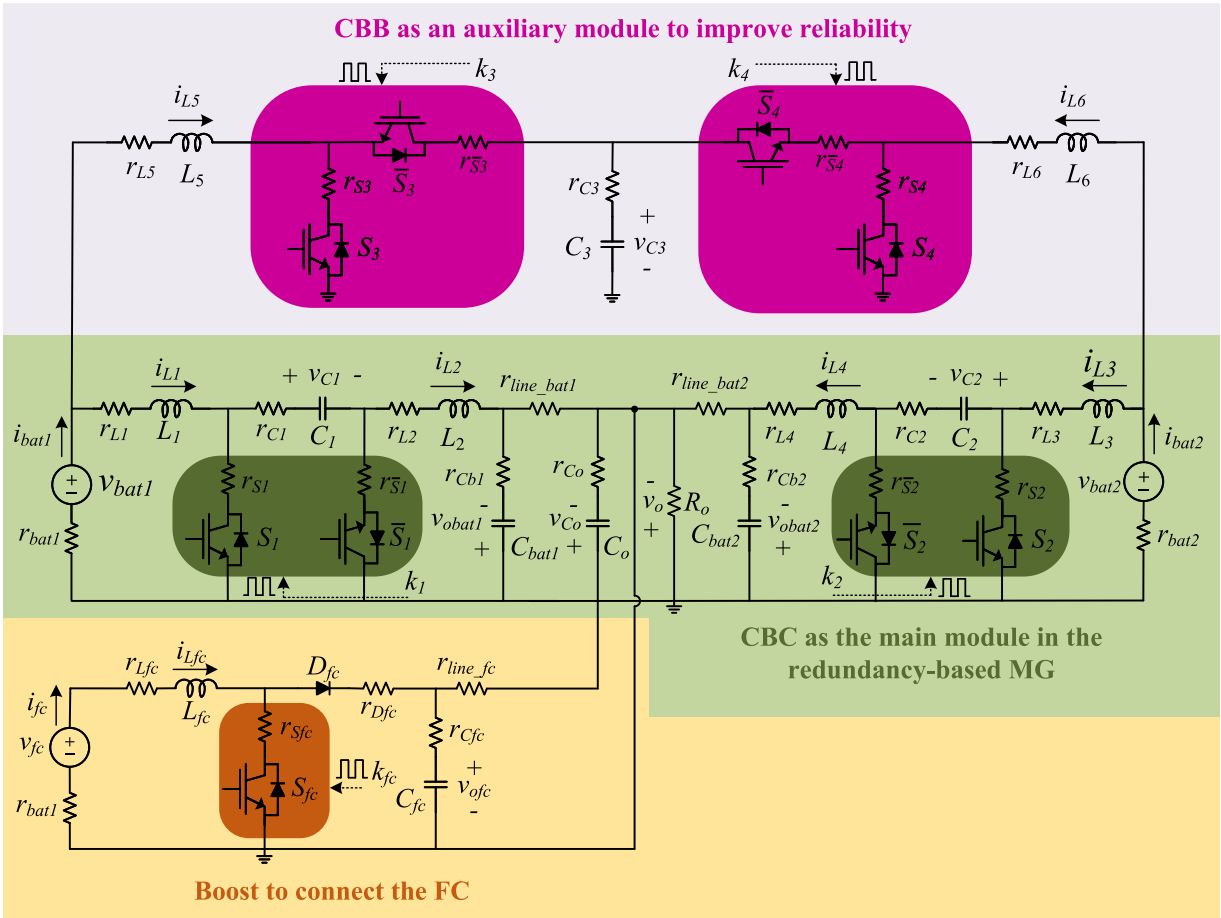

FIGURE 5. Redundancy-based MG that will receive the secondary voltage control for the EMS.

A secondary voltage control can be formulated for a dc load operating at a specific voltage level during variations, maintenance, or failures in the DGs, preventing voltage fluctuations in the main dc-link. As the SoC-sharing function developed in [4] operates based on voltage deviation, addressing voltage restoration emerges as a significant issue in designing the operation of the dc MG to interface with sensitive loads that require a predefined voltage value. Consequently, there is an improvement in the reliability of the proposed redundancy-based dc MG.

A. SECONDARY VOLTAGE CONTROL FOR THE FC OPERATION

The authors designed a droop controller for the management of the FC, as indicated as follows:

$$i_{fc\_ref} = I_{fc\_rated}\left(\frac{v_{ref}}{\Delta v_o} - \frac{v_o}{\Delta v_o}\right) n_{di} \tag{8}$$

where i_{fc_ref} is the current reference and I_{fc_rated} is the rated current of the FC, v_{ref} is the dc-link voltage reference, Δv_o is voltage deviation, and n_{di} is the low-pass filter to introduce a delay in the current step. Although the output voltage from Cuk is negative, the probe from the voltage sensor is set to indicate a positive value. In this context, the droop controller is supposed to operate in a range of $[v_{ref} - \Delta v_o; v_{ref}]$. However, the authors proposed the secondary voltage control for the redundancy-based dc MG operates at a predefined voltage value of v_{ref}. Thus, in the expression of (9), there is a required voltage shift on the dc-link, denoted as δv_{fc}, which depends on the current i_{fc_pu}. This shift ensures that the dc-link voltage remains constant despite variations in load conditions. The expression for δv_{fc} is given by

$$\delta v_{fc} = (v_{ref} - v_o) n_{dv} = (i_{fc\_pu} \Delta v_o) n_{dv}. \tag{9}$$

In (9), i_{fc_pu} is the per unit (p.u.) current of the FC and n_{dv} is a low pass-filter to guarantee a delay in the secondary voltage. Thus, after the steady-state of the EMS operation, the secondary voltage control acts to introduce a term δv to correct the voltage deviation, as shown in (10). As a result, in the new expression of (10), δv is the average of δv_{fc}, δv_{bat1} and δv_{bat2} (Subsection IV-B will explain the δv_{bat} calculation), while $i_{fc\_ref\_\delta v}$ is the FC current reference designed with the secondary voltage control

$$i_{fc\_ref\_\delta v} = \frac{I_{fc\_rated}}{\Delta v_o}\left(v_{ref} - v_o + \delta v\right) n_{di}. \tag{10}$$

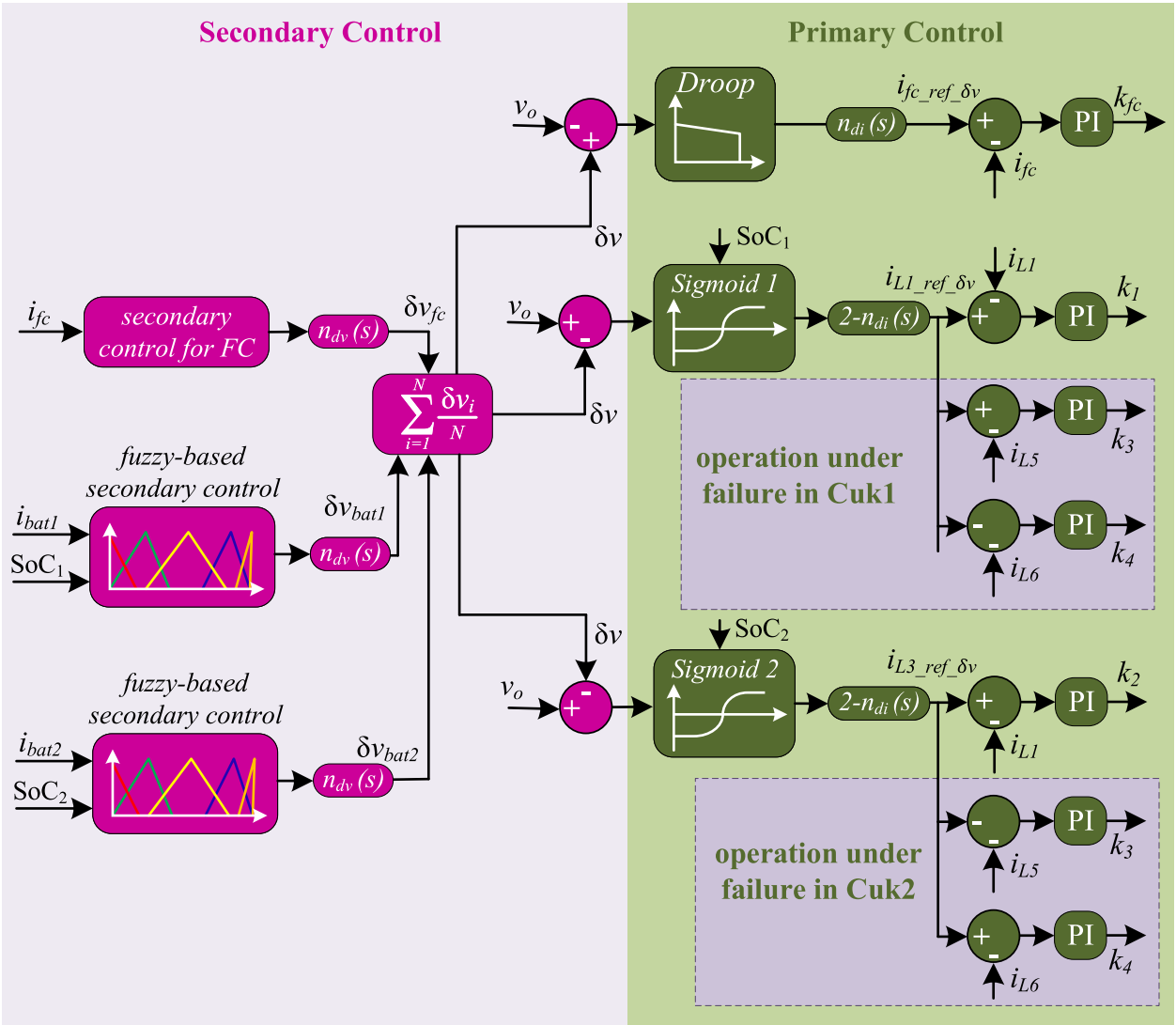

FIGURE 6. EMS modified by the fuzzy-based secondary voltage control.

Later, a PI controller is designed to provide the duty-cycle, k_{fc}, by comparing $i_{fc\_ref\_\delta v}$ with the measured current from the FC.

B. FUZZY-BASED VOLTAGE SECONDARY CONTROL FOR THE EMS OF THE BESS UNITS

The SoC equalization strategy designed for the BESS units is named SoC-sharing, as indicated by [4]. Thus, the BESS unit is coordinated by a Sigmoid function with SoC and the dc-link voltage as input. In the proposed approach, there is a Sigmoid 1 for BESS1 and a Sigmoid 2 for the BESS2. The expression (11) defines the current reference i_{L_ref} for each BESS. As the CBC is the main module of the redundancy-based dc MG, i_{L1_ref} and i_{L3_ref} represent the EMS for BESS1 and BESS2, respectively. As a result, i_{L1_ref} is identical to i_{bat1_ref}, while i_{L3_ref} is identical to i_{bat2_ref}. The inputs are the dc-link voltage v_o, with SoC$_1$ for BESS1 and SoC$_2$ for BESS2

$$i_{L\_ref} = I_{bat\_rated} \left[\frac{2}{1 + \exp\left(\frac{v_o - v_{ref} - \Delta v_o}{\Delta v_o} - \text{SoC} \right) p} - 1 \right] (2 - n_{di}). \quad (11)$$

In this equation, I_{bat_rated} represents the BESS rated current, $(2 - n_{di})$ acts as a high-pass filter to implement a rapid response in the BESS unit, and p is set to 10 (as indicated by [4]).

In Fig. 7, the power flow redirection from CBC to CBB is indicated when there is an unpredictable event in Cuk1 or Cuk2. Since the redundancy-based dc MG is symmetrical, the power flow from BESS1 through CBB is evaluated in the case of a failure in Cuk1. However, the power flow from BESS2 in the event of a Cuk2 malfunction would exhibit similar behavior. As depicted in Fig. 7, CBB receives the reference

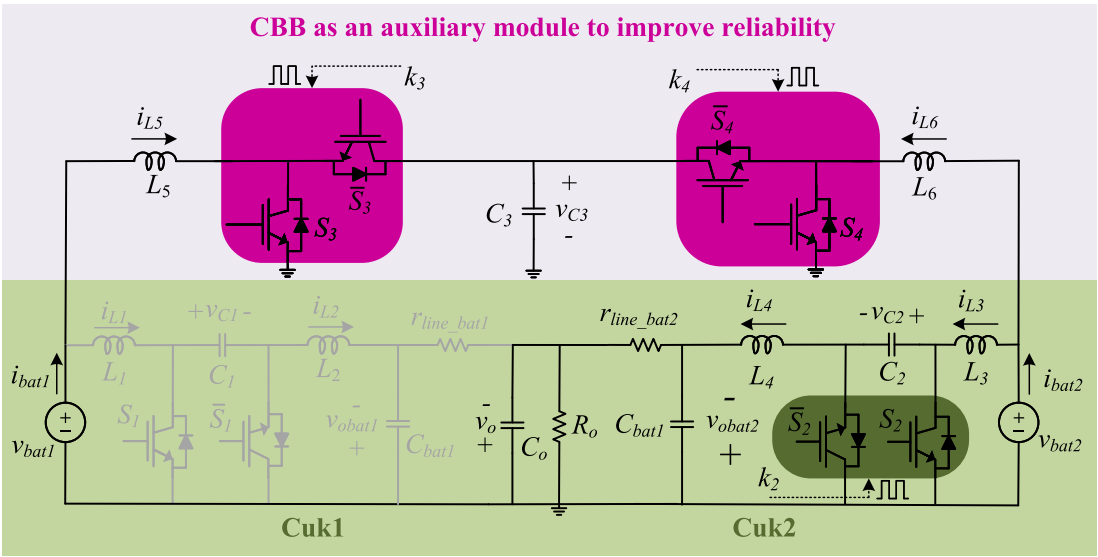

FIGURE 7. Example of a power flow redirection in the event of a failure in Cuk1.

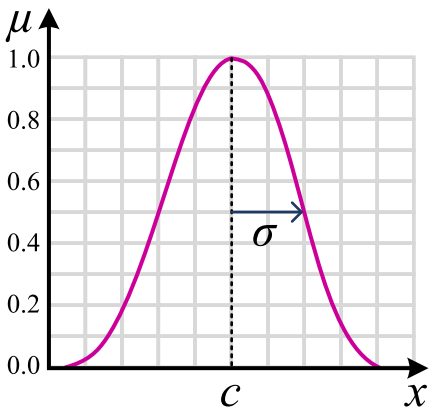

FIGURE 8. Illustration of a Gaussian Function.

value from Sigmoid 1 in the expression (11); then, i_{bat1_ref} becomes equals to i_{L5_ref}, which is also identical to $-i_{L6\_ref}$.

For achieving the SoC equalization, the main dc-link is supposed to operate within an interval $[v_{ref}\text{-}\Delta v_o, v_{ref}]$. Thus, the authors introduce a fuzzy-based secondary control to set the voltage to v_{ref}, even in the event of load variation, failure or maintenance in the DGs. This fuzzy-based secondary voltage control is achieved through an analysis of the Sigmoid function behavior. For example, if the BESS units are providing the maximum possible current, the δv_{bat} is likely higher due to the significant amount of power in the dc-link. In this scenario, the SoC assists the fuzzy-based method in determining the δv_{bat}.

Conversely, if the current from the BESS unit is maximized for charging, it indicates that the redundancy-based dc MG is operating under a low load. Consequently, the fuzzy-based method sets a lower δv_{bat} also taking into account the SoC of the BESS unit. From the membership for the fuzzy-based method, the authors designed a Gaussian function μ, as shown

TABLE 5. Gaussian Membership of μ_{ibat}

	μ_{ibat}				
	I	II	III	IV	V
σ (p.u.)	0.3	0.3	0.3	0.3	0.3
c (p.u.)	−1	−0.5	0	0.5	1

TABLE 6. Gaussian Membership of μ_{SoC}

	μ_{SoC}				
	1	2	3	4	5
σ (%)	10	10	10	10	10
c (%)	0	25	50	75	100

TABLE 7. Gaussian Membership of $\mu_{\delta vbat}$

	$\mu_{\delta vbat}$						
	A	B	C	D	E	F	G
σ_1 (V)	−9.5	−3.5	2.5	8.5	14.5	20.5	26.5
c_1 (V)	1.5	1.5	1.5	1.5	1.5	1.5	1.5
σ_2 (V)	−6.5	−0.5	5.5	11.5	17.5	23.5	29.5
c_2 (V)	1.5	1.5	1.5	1.5	1.5	1.5	1.5

in (12), with σ being the standard deviation and c representing the center position (mean), as indicated in Fig. 8.

$$\mu = \exp \frac{-(x-c)^2}{2\sigma^2}. \tag{12}$$

Thus, Table 5 indicates the membership function parameters for μ_{ibat}, which are defined in the first graph of Fig. 9. Considering the μ_{ibat}, each Gaussian function is proportionally spaced with a mean c of −1 p.u. for "I," −0.5 p.u. for "II," 0 p.u. for "III," 0.5 p.u. for "IV," and 1 p.u. for "V" and constant σ (0.3 p.u.)

In addition, as another input from the fuzzy-based method is the SoC, Table 6 indicates the parameters for the membership function μ also defined according to (12) as μ_{SoC} and illustrated in the second graph of Fig. 9. The membership

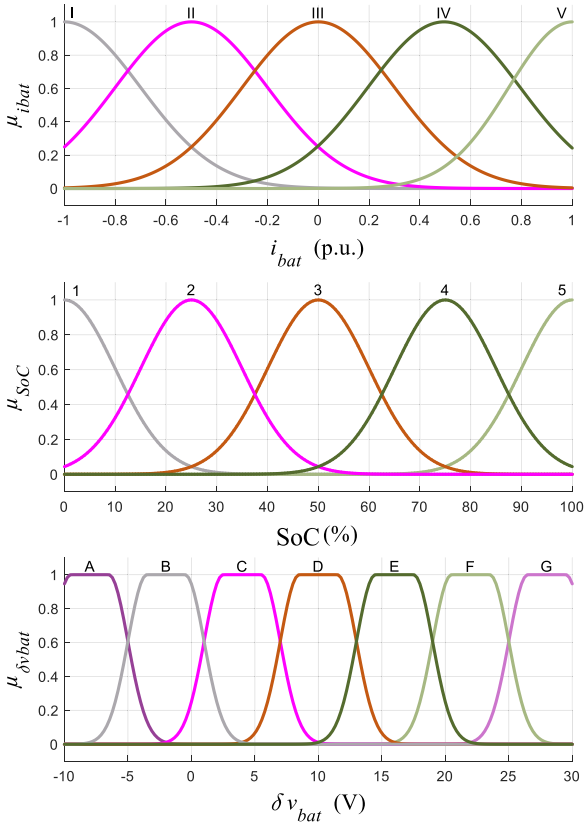

FIGURE 9. Membership functions from top to bottom: i_{bat} (p.u.) as input, SoC (%) as input, δv_{bat} (V) as output.

TABLE 8. Rules to Design the Fuzzy-Based Voltage Secondary Control

	δv_{bat}				
SoC	**I**	**II**	**III**	**IV**	**V**
1	D	E	F	F	G
2	C	D	E	F	F
3	B	C	D	E	F
4	B	B	C	D	E
5	A	B	B	C	D

function is equally spaced with a mean c of 0% for "1," 25% for "2," 50% for "3," 75% for "4," and 100% for "5," while the parameter σ is set as constant (50 %)

In sequence, the membership $\mu_{\delta vbat}$ is the output, as represented at the bottom of Fig. 9 and defined in Table 7. For this membership, the authors designed it with a combination of two Gaussian functions, each one representing the shape of one side of the membership function. Thus, σ_1 and c_1 are the standard deviation and mean of the left Gaussian function, while σ_2 and c_2 are the parameters of the right Gaussian function. For c_1 and c_2 for each Gaussian function, they are equally spaced, and σ_1 and σ_2 are kept as constant (1.5 V).

In this context, the fuzzy-based method receives the current from BESS unit and its respective SoC to produce the term δv_{bat}. First, the measured i_{bat} (p.u.) and SoC are processed by the fuzzifiers into fuzzy variables. Later, μ_{ibat} and

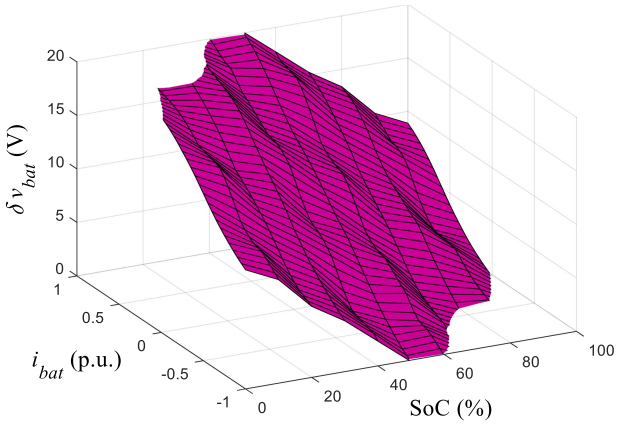

FIGURE 10. Secondary voltage control surface for the BESS unit.

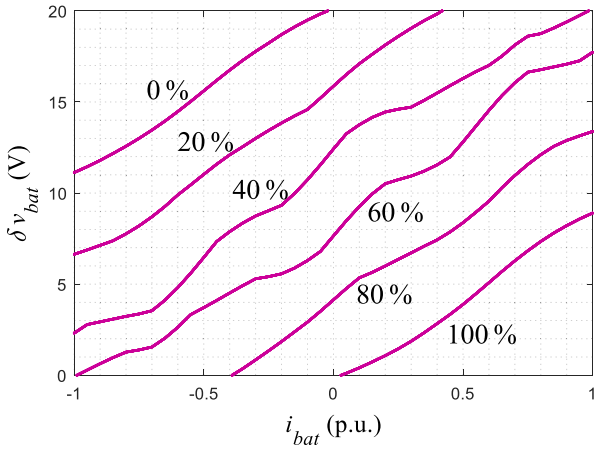

FIGURE 11. Relationship between i_{bat} and δv_{bat} for varying SoC levels.

μ_{SoC} are derived from the membership functions, as shown in Fig. 9.

Then, Mamdani's fuzzy inference system generates the output values considering the fuzzy rules in Table 8 and the membership function of δv_{bat}. Finally, it is obtained the aggregated fuzzy set of δv_{bat}, followed by defuzzification using the center of gravity method to calculate the numerical value of δv_{bat}.

For this fuzzy-based method, according to [37] and [38], Gaussian functions have the capability to give smoother results. Since the Sigmoid function is tailored for the SoC equalization process due to its smoothness, the design of membership functions with Gaussian functions demonstrates better performance in the secondary voltage control for estimating the term δv_{bat}. In this context, δv_{bat1} represents the voltage deviation of BESS1, while δv_{bat2} corresponds to the voltage deviation of BESS2. Both parameters undergo processing through a low-pass filter denoted as n_{dv} to apply a delay into the secondary voltage control.

In Fig. 10, the surface produced by the fuzzy-based secondary voltage control defines δv_{bat} (ranging from 0 to 20 V). This is determined based on i_{bat} (indicated within the interval $[-1, 1]$) and SoC (ranging from 0% to 100%). Therefore,

this surface represents the strategy for obtain the parameters necessary to set the voltage at a predefined value.

To facilitate the interpretation of the surface illustrated in Fig. 10, 2-D slices are presented in Fig. 11, where i_{bat} is plotted as a function of δv_{bat} for different constant SoC levels (0%, 20%, 40%, 60%, 80%, and 100%).

From Fig. 11, it can be observed that when the BESS units are fully charged (SoC = 100%), the system operates with $i_{bat} > 0$ A, indicating that the fully charged BESS units are delivering power to the dc-link, which is subjected to a low dc load. As a result, the voltage deviation δv_{bat} remains small (ranging from 0 to 10 V). In contrast, as the SoC decreases, the curves shift progressively. For instance, at SoC = 0 %, the variation of δv_{bat} occurs between 10 and 20 V, reflecting a higher power demand from the dc load. Consequently, the voltage deviation at v_o increases, and since the BESS units are depleted, they absorb power, resulting in $i_{bat} < 0$ A.

Finally, the average of δv_{fc}, δv_{bat1} and δv_{bat1} defines the term δv, as also demonstrated in Fig. 6 In sequence, the SoC-sharing function is modified by the term δv as follows:

$$i_{L\_ref\_\delta v} = I_{bat\_rated} \left[\frac{2}{1 + \exp\left(\frac{v_o - v_{ref} - \Delta v_o - \delta v}{\Delta v_o} - \text{SoC} \right) p} - 1 \right] (2 - n_{di}). \tag{13}$$

In this equation, BESS1 operates with the current reference $i_{L1\_ref\_\delta v}$, while BESS2 receives the current reference $i_{L3\_ref\_\delta v}$. In addition, in case of a failure in Cuk1, $i_{L5\_ref\_\delta v}$ is responsible for the reference of BESS1, while $i_{L6\_ref\_\delta v}$ is responsible for the reference of BESS2 in the event of a failure in Cuk2. Later, the measured currents i_{L1}, i_{L3}, i_{L5} and i_{L6} are processed by a comparator with their corresponding current references to generate PWM signals through PI controllers.

V. EFFICIENCY EVALUATION

This section assesses the efficiency of the redundancy-based dc MG based on the average values of the BESS unit currents (I_{bat1} and I_{bat2}) and voltages (V_{bat1} and V_{bat2}), as well as the average FC current (I_{fc}) and average FC voltage (V_{fc}). Thus, the power from BESS units and FC are defined as follows:

$$\begin{cases} P_{bat1} = V_{bat1} I_{bat1} = V_{bat1}(I_{L1} + I_{L5}) \\ P_{bat2} = V_{bat2} I_{bat2} = V_{bat2}(I_{L3} + I_{L6}) \\ P_{fc} = V_{fc} I_{fc}. \end{cases} \tag{14}$$

Thus, in the case where $P_{bat1} > 0$ and $P_{bat2} < 0$, the efficiency is given as follows:

$$\eta = \frac{P_{load} - P_{bat2}}{P_{fc} + P_{bat1}} \tag{15}$$

where P_{load} represents the power consumed by the load.

Similarly, for the case where $P_{bat1} < 0$ and $P_{bat2} > 0$, the efficiency is expressed as follows:

$$\eta = \frac{P_{load} - P_{bat1}}{P_{fc} + P_{bat2}}. \tag{16}$$

Finally, for the scenario where both $P_{bat1} > 0$ and $P_{bat2} > 0$, the efficiency is determined as follows:

$$\eta = \frac{P_{load}}{P_{fc} + P_{bat1} + P_{bat2}}. \tag{17}$$

Since the BESS units can either supply or absorb power, as indicated in (18), P_{bat1in} and P_{bat2in} denote the power absorbed by BESS1 and BESS2, respectively, while $P_{bat1out}$ and $P_{bat2out}$ represent the power delivered by BESS1 and BESS2, respectively.

$$\begin{cases} P_{bat1in} = 0.5(P_{bat1} + |P_{bat1}|) \\ P_{bat2in} = 0.5(P_{bat2} + |P_{bat2}|) \\ P_{bat1out} = 0.5(P_{bat1} - |P_{bat1}|) \\ P_{bat2out} = 0.5(P_{bat2} - |P_{bat2}|). \end{cases} \tag{18}$$

When $P_{bat1} > 0$ and $P_{bat2} > 0$, the BESS units are supplying power, leading to $P_{bat1in} = P_{bat1}$ and $P_{bat2in} = P_{bat2}$, while $P_{bat1out} = 0$ and $P_{bat2out} = 0$. On the other hand, when the BESS units are absorbing power, i.e., $P_{bat1} < 0$ and $P_{bat2} < 0$, the conditions in (18) result in $P_{bat1in} = 0$, $P_{bat2in} = 0$, $P_{bat1out} = P_{bat1}$, and $P_{bat2out} = P_{bat2}$.

Thus, the efficiency of the redundancy-based DC MG can be determined as follows:

$$\eta = \frac{P_{load} - P_{bat1out} - P_{bat2out}}{P_{fc} + P_{bat1in} + P_{bat2in}} = \frac{P_{out}}{P_{in}} \tag{19}$$

where P_{in} represents the total supplied power and P_{out} denotes the consumed power.

Finally, the efficiency analysis presented in this work is based on the ratio between output (P_{out}) and input power (P_{in}), as defined in (19), which inherently includes the effects of conduction losses, switching losses, and other internal system inefficiencies. Therefore, it provides a practical and comprehensive estimation of overall system performance without the need for explicitly modeling dead-time, snubber circuits, or semiconductor losses.

VI. STABILITY ANALYSIS

The stability analysis for the redundancy-based dc MG operating with a fuzzy-based secondary voltage control is evaluated by the Lyapunov's indirect method. First of all, the average redundancy-based DC MG is represented in subsection VI-A. In sequence, the Jacobian matrix is applied to obtain the movement of the eigenvalues, as proposed by [30].

Regarding the operation of the main module (CBC), Section VI-B presents the behavior of the eigenvalues in relation to dc load variation and SoC equalization. Subsequently, Section VI-C analyzes dc load variation under constant SoC conditions, during which power flow is redirected from the CBC to the CBB module. Finally, Section VI-D evaluates the stability considering the power contributions from both the BESS units and the FC.

A. REDUNDANCY-BASED DC MG AVERAGE MODEL

The analytical model in (20), shown at the bottom of this page, from the conventional dc MG in [30] was revised to incorporate the interaction among CBC, CBB, and the Boost converter, incorporating the SoC-sharing function and a droop controller modified by the voltage secondary control. Since the fuzzy-based voltage control is designed for the BESS units, the fuzzy surface is approximated by the Fourier series $\delta v_{bat}(i_{bat})$ for constant SoC. Consequently, the eigenvalues used to assess stability are derived from the solution of the Jacobian matrix in (20).

The common coupling voltage ($\dot{v}_o$) is derived from (21) shown at the bottom of this page, with the derivation process detailed in the Appendix. Furthermore, Figs. 12 and 13 illustrate the control schemes for the FC and BESS units, respectively, which are essential for obtaining the model in (20).

In (20), the state vector $\boldsymbol{x}_{red}$ represents the redundancy-based topology and is defined as shown in the matrix $[i_{L1}\ \ i_{L2}\ \ v_{C1}\ \ i_{L3}\ \ i_{L4}\ \ v_{C2}\ \ i_{L5}\ \ i_{L6}\ \ v_{C3}\ \ v_o]^T$. Meanwhile, the error of currents are denoted by $\dot{\boldsymbol{e}}_{iL1}, \dot{\boldsymbol{e}}_{iL3}, \dot{\boldsymbol{e}}_{iL5}$, $\dot{\boldsymbol{e}}_{iL6}$, and $\dot{\boldsymbol{e}}_{fc}$.

The input vectors $\boldsymbol{u}_{red}$ and $\boldsymbol{u}_{fc}$ for the redundancy-based topology and FC converters are defined as $[v_{bat1}\ \ v_{bat2}\ \ v_o]^T$ and $[v_{fc}]^T$, respectively. Notably, the state vector $\boldsymbol{x}_{fc}$, representing the FC, is defined as $[i_{fc}\ \ v_o]^T$, with careful consideration to avoid the DC-link voltage, as indicated by the vector indices.

The state space matrices $\boldsymbol{A}_{red}(k_1, k_2, k_3, k_4)$ and $\boldsymbol{B}_{red}(k_1, k_2, k_3, k_4)$ pertain to the redundancy-based topology. The matrix indices (1:9,1:10) are selected to exclude parameters related to $\dot{v}_o$, whereas (10,1:10) explicitly include them. Similarly, $\boldsymbol{A}_{fc}$ and $\boldsymbol{B}_{fc}$, representing the FC state space model, incorporate the duty-cycle k_{fc} in their expressions, and matrix indices are carefully chosen to account for or exclude parameters associated with dc-link voltage and $\dot{v}_o$.

The state variables $\delta\dot{v}_{bat1}$, $\delta\dot{v}_{bat2}$, and $\delta\dot{v}_{fc}$ characterize the voltage secondary control. Additionally, time constants τ_i and τ_v are introduced as parameters for the low-pass filters in the current delay and voltage secondary control, respectively. Lastly, the common coupling voltage is indicated in (21), where the term $(-\frac{v_o}{R_o C_{eq}})$ represents the integration of the FC and CBC converters, showcasing the interplay between voltage and resistance parameters. Here, C_{eq} denotes the equivalent output capacitance (see Appendix).

B. EVALUATION OF SOC EQUALIZATION WITH DC LOAD VARIATION IN THE MAIN MODULE OPERATION

In this procedure, the initial values for each SoC are $\mathrm{SoC}_1 = 90\,\%$ and $\mathrm{SoC}_2 = 10\,\%$. The DC load variation generates a power P_{load} in the main dc-link ranging from 250 to 1000 W. Subsequently, the SoC equalization is evaluated with $\Delta\mathrm{SoC} = \mathrm{SoC}_1 - \mathrm{SoC}_2 \rightarrow 0\,\%$) for each step of analysis.

Finally, Fig. 14 indicates the maximum real part of the eigenvalues $max(Re(\lambda_i))$. In this figure, the redundancy-based dc MG is stable for P_{load} lower than 950 W. Notably, values higher than 950 W presents some positive eigenvalues, characterizing an unstable operation. The reason for this is that the power sources (BESS units and FC) reach their maximum operating capacity. Consequently, when the load power (P_{load}) exceeds 950 W, the redundancy-based dc MG exhibits instability.

$$\begin{bmatrix} \dot{v}_o \\ \dot{\boldsymbol{x}}_{red}^{(1:9)} \\ \dot{e}_{iL1} \\ \dot{i}_{L1\_ref} \\ \dot{e}_{iL3} \\ \dot{i}_{L3\_ref} \\ \dot{e}_{iL5} \\ \dot{e}_{iL6} \\ \delta\dot{v}_{bat1} \\ \delta\dot{v}_{bat2} \\ \dot{\boldsymbol{x}}_{fc}^{(1:2)} \\ \dot{e}_{fc} \\ \dot{i}_{fc\_ref} \\ \delta\dot{v}_{fc} \end{bmatrix} = \begin{bmatrix} DC_{coupled} \\ \boldsymbol{A_{red}}(k_1, k_2, k_3, k_4)^{(1:9,1:10)}\boldsymbol{x_{red}} + \boldsymbol{B_{red}}(k_1, k_2, k_3, k_4)^{(1:9,1:2)}\boldsymbol{u_{red}} \\ 2i_{bat1\_sig} - i_{L1\_ref} - i_{L1} \\ \frac{1}{\tau_i}[i_{bat1\_sig} - i_{L1\_ref}] \\ 2i_{bat2\_sig} - i_{L3\_ref} - i_{L3} \\ \frac{1}{\tau_i}[i_{bat2\_sig} - i_{L3\_ref}] \\ i_{L5\_ref} - i_{L5} \\ i_{L6\_ref} - i_{L6} \\ \frac{1}{\tau_v}[\delta v_{bat1\_out} - \delta v_{bat1}] \\ \frac{1}{\tau_v}[\delta v_{bat2\_out} - \delta v_{bat2}] \\ (\boldsymbol{A}_{fc10}^{(1,1:2)} + k_{fc}\boldsymbol{A}_{fck}^{(1,1:2)})\boldsymbol{x}_{fc} + (\boldsymbol{B}_{fc0}^{(1,1)} + k_{fc}\boldsymbol{B}_{fck}^{(1,1)})\boldsymbol{u}_{fc} \\ i_{fc\_ref} - i_{fc} \\ \frac{1}{\tau_i}[i_{fc\_droop} - i_{fc\_ref}] \\ \frac{1}{\tau_v}[\delta v_{fc\_out} - \delta v_{fc}] \end{bmatrix} \tag{20}$$

$$DC_{coupled} = (\boldsymbol{A}_{red}(k_1, k_2, k_3, k_4)^{(10,1:10)})\boldsymbol{x}_{red} + (\boldsymbol{B}_{red}(k_1, k_2, k_3, k_4)^{(10,1:10)})\boldsymbol{u}_{red} - (\boldsymbol{A}_{fc0}^{(2,1:2)} + k_{fc}\boldsymbol{A}_{bfck}^{(2,1:2)})\boldsymbol{x}_{fc} - (\boldsymbol{B}_{fc0}^{(2,1)} + k_{fc}\boldsymbol{B}_{fck}^{(2,1)})\boldsymbol{u}_{fc}. - \left(-\frac{v_o}{R_o C_{eq}}\right) \tag{21}$$

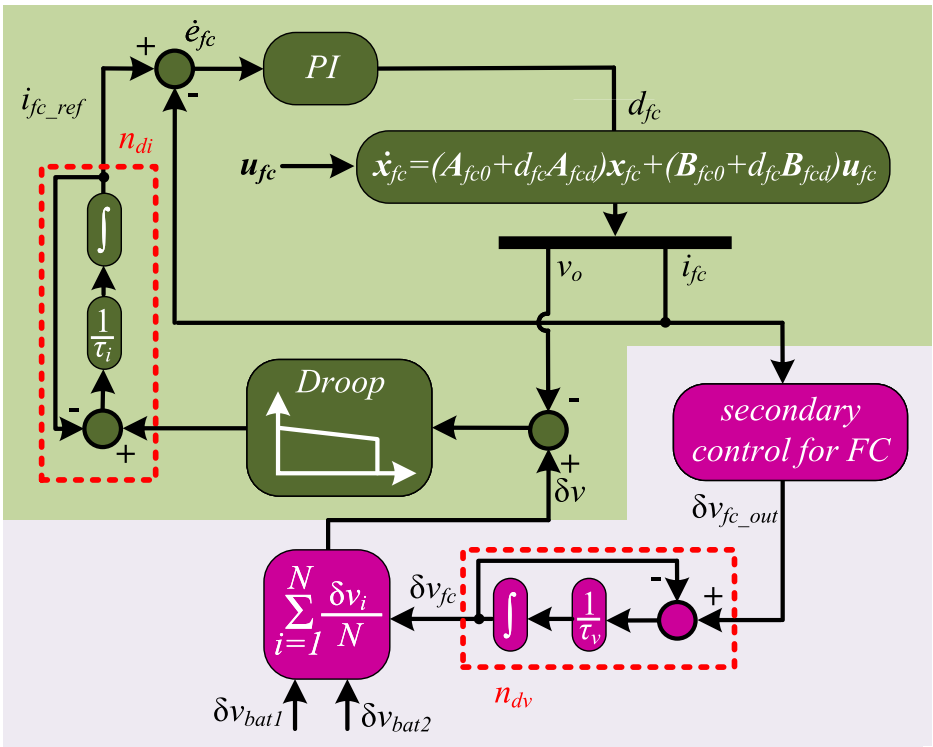

FIGURE 12. Control strategy for the FC to derive the average model of the redundancy-based dc MG.

C. EVALUATION OF POWER FLOW REDIRECTED FROM CBC TO CBB

Finally, for the second case, the $SoC_1 = 80\,\%$ and $SoC_2 = 20\,\%$ are constant for the complete stability analysis. In sequence, the dc load varies to produce P_{load} ranging from 250 to 1000 W, and the power flow is redirect from Cuk1 to CBB, resulting in $i_{L1} = 0$. In this context, Fig. 15 indicates the movement of the eigenvalues in the complex plane obtained from the state variables i_{L1}, i_{L2}, v_{C1}, i_{L3}, i_{L4}, v_{C2} are i_{L5}, which play a crucial role in defining stability. Thus, Fig. 15 demonstrates that the eigenvalues start to present instability when the power produced exceeds 980 W. This limitation stems from the power sources (BESS units and FC) having already reached their maximum output capacity.

D. EVALUATION OF POWER CONTRIBUTION FROM BESS UNITS AND FC

In the final case, the objective is to evaluate the influence of power sources (BESS units and FC) on the stability analysis. A power variation is applied to the BESS units ($P_{bat1} + P_{bat2}$), starting from 0 W and increasing up to 700 W, while the power supplied by the FC (P_{fc}) ranges from 0 to 1000 W. In addition, the power demand on the dc-link is fixed at 400 W, with $SoC_1 = 20\,\%$ and $SoC_2 = 80\,\%$. In this scenario, the dc MG exhibits instability when the BESS units provide approximately 0 W or when the FC supplies nearly 0 W—making it impossible to sustain DC-link operation. In all other cases, $\max(\mathrm{Re}(\lambda_i))$ remains negative, as illustrated in Fig. 16.

VII. EXPERIMENTAL RESULTS

The experimental validation of the proposed redundancy-based dc MG topology and its EMS was conducted using a HIL setup. The HIL platform integrates SpeedGoat for real-time power stage emulation and dSPACE for executing the EMS, secondary voltage control and controller algorithms, as indicated in Fig. 17. This configuration enables real-time closed-loop testing, ensuring the accuracy of the proposed system under dynamic operating conditions.

The schematic illustrating the board connections is presented in Fig. 18. In this setup, the dSPACE1006 multi-processor system, featuring an AMD Opteron™ processor, retrieves analog signals from SpeedGoat through the 16-bit A/D board DS2004 and generates PWM signals via the digital board DS4004. Subsequently, the measurements related to the redundancy-based DC MG are obtained from SpeedGoat, which is powered by a performance-core Intel Core™ i3 FPGA 100 k, using the 16-bit analog output board IO110, while the PWM signals are acquired through the digital board IO316.

In the HIL implementation, the PWM signals operate at a switching frequency of 10 kHz, the FC has a rated power of 1 kW with a rated current of 20 A. The BESS unit is characterized by a capacity of 60 Ah, a rated voltage of 36 V, and a maximum current of 10 A. In addition, the semiconductor models were based on the IGBT module SKM75GB063D and the fast recovery diode DSEI 2X31-06 C, which were used to emulate realistic switching behavior in the SpeedGoat platform.

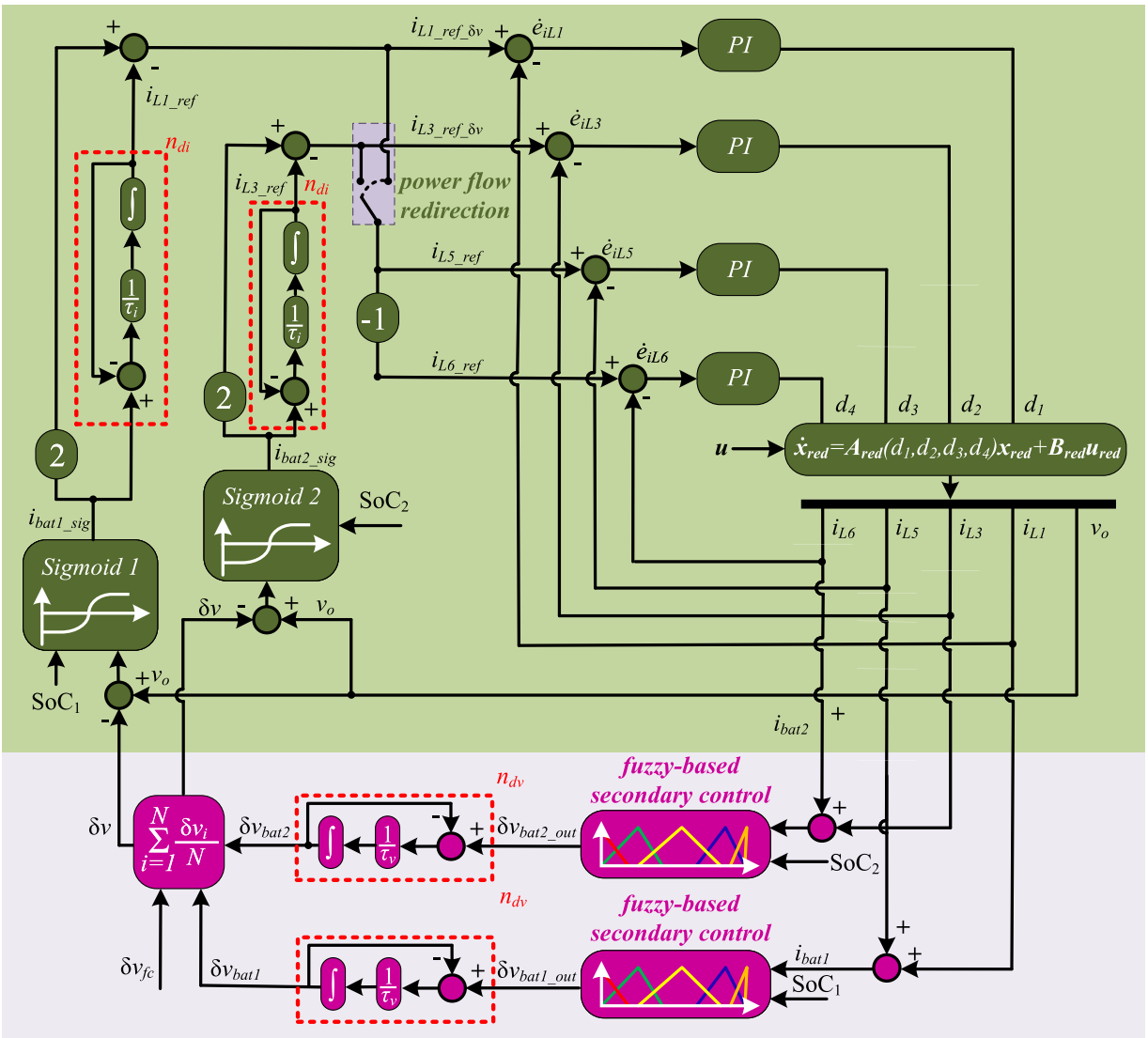

FIGURE 13. Control strategy for the BESS units to derive the average model of the redundancy-based dc MG.

The predefined voltage reference v_{ref} is set at 170 V, and the EMS has a range of $\Delta v_o = 20$ V, which is corrected by the secondary voltage control.

In the redundancy-based DC MG shown in Fig. 5, the parameters were considered along with their parasitic losses, as outlined in Table 9.

A. SOC EQUALIZATION IN MAIN MODULE: EXPERIMENTAL AND SIMULATION COMPARISON

The scenario was evaluated with the main module CBC in operation to achieve the SoC equalization from the BESS units. The initial SoC values were set as $\text{SoC}_1 = 90\,\%$ and $\text{SoC}_2 = 70\,\%$, while the CBB was on standby i.e. $i_{L5} = 0$ A and $i_{L6} = 0$ A. To speed up the SoC balancing process during the experimental procedure, the capacity of the BESS units was reduced by a factor of 500. This adjustment allowed the SoC to vary more rapidly, enabling the complete evaluation of the equalization strategy within a shorter time frame, while maintaining the dynamics and behavior of the control system. In conjunction with the CBC, the FC operated to supply the main DC-link.

Thus, the waveforms of the main dc-link voltage v_o, FC current i_{fc}, inductance currents i_{L1} and i_{L3}, SoC_1 and SoC_2 are indicated in Fig. 19. Also, in Fig. 19, the dashed line with circular markers represents the simulation results from Simulink, while the continuous line is obtained from experimental results on the HIL platform.

In addition, throughout the operation, there is an increment of load steps in the main dc-link with a value $\Delta P_{load} \approx 250$ W. The BESS units respond rapidly to compensate for the transient, while the FC has a slower response, protecting its membranes. At 5 s, there is maintenance in BESS1 that does not impact SoC equalization, occurring at 32 s since the SoC-sharing function operates in a decentralized manner. Furthermore, the FC undergoes scheduled maintenance at 27 s, which does not impact the dc-link voltage.

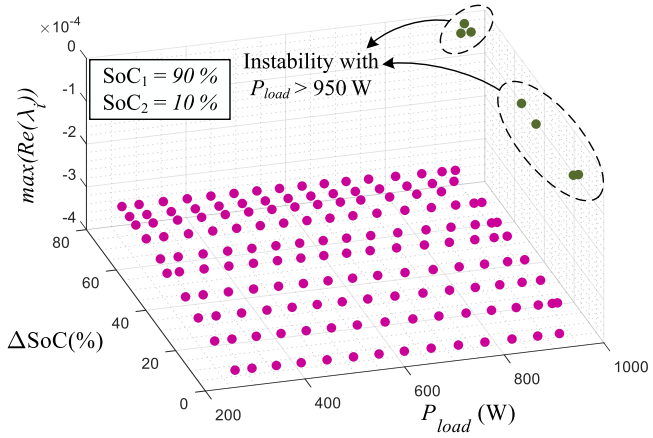

FIGURE 14. max($Re(\lambda_i)$) as a function of P_{load} and the equalization process when ΔSoC $\rightarrow$ 0 %.

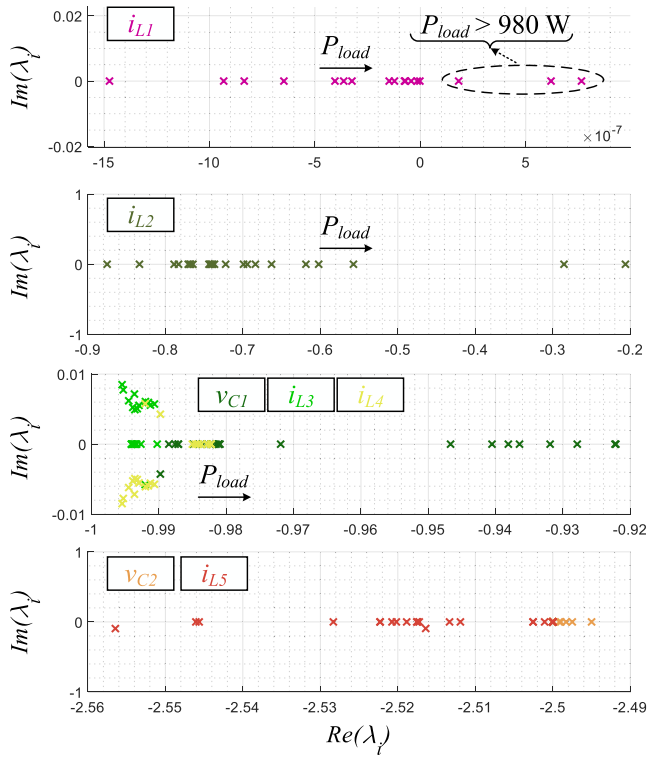

FIGURE 15. Movement of eigenvalues in the complex plane with constant SoC (SoC_1 = 80 % and SoC_2 = 20 %).

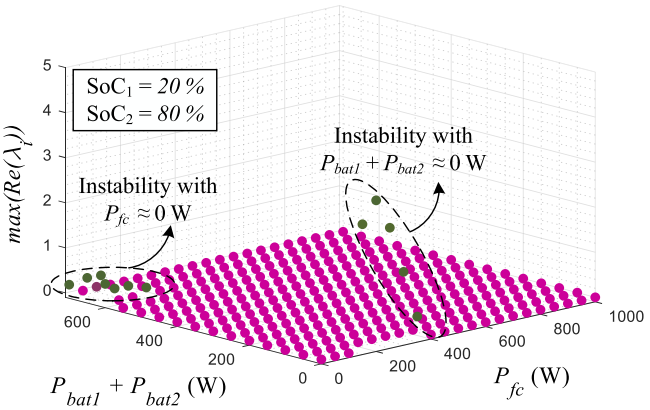

FIGURE 16. max($Re(\lambda_i)$) as a function of the total power from BESS units and FC.

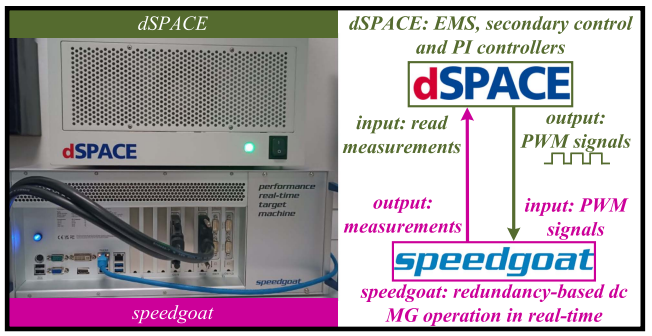

FIGURE 17. Lab-scale prototype.

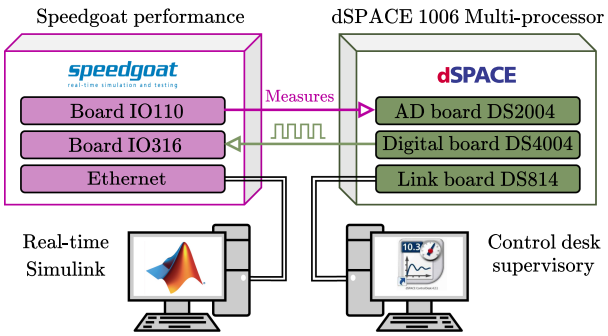

FIGURE 18. Board connections schematic.

Regarding to the secondary voltage control, it is activated at 3 s, which impact in set the voltage v_o at 170 V. When maintenance is performed on BESS1 or FC, the EMS excludes the respective δv_{fc} or δv_{bat} from the average calculation to obtain δv. Thus, the voltage secondary restoration result remains unaffected. Since the fuzzy-based method is not continuous and nebulous, the v_o has an operation surrounding 170 V. However, the main dc-link with the secondary voltage control behaves in the range from 168 to 172 V, with a 1.1% of deviation, resulting in a satisfactory performance that does not impact the sensitive load in operation at the redundancy-based dc MG. As a result, during the load variation and maintenance of BESS1 and FC, the voltage from the main DC-link remain in the aforementioned interval. Finally, based on (19), the overall efficiency for this experimental result is approximately $\eta = 95.2\,\%$.

B. OPERATION UNDER FAILURE IN CUK: POWER FLOW REDIRECTION FROM CBC TO CBB

Finally, this procedure evaluates a failure in Cuk1, resulting in power flow redirection from CBC to CBB. Fig. 20 indicates the waveforms of the main dc-link voltage v_o, FC current i_{fc}, inductance currents flowing in CBC (i_{L1} and i_{L3}) and CBB (i_{L5} and i_{L6}), BESS currents i_{bat1} and i_{bat2}, and SoC_1 set as an initial value at 80 % and SoC_2 at 20%. During the operation,

TABLE 9. Parameters From the Redundancy-Based DC MG

Component	*Value*
Inductances (L_1, L_2, L_3, L_4, L_5, L_6)	4.8 mH
Inductances (L_{fc})	4.8 mH
C_1 and C_2	130 μF
C_3 and C_o	470 μF
C_{fc}, C_{bat1} and C_{bat2}	100 μF
Parasitic Losses	***Value***
$r_{L1} = r_{L2} = r_{L3} = r_{L4} = r_{L5} = r_{L6}$	150 $m\Omega$
r_{Lfc}	150 $m\Omega$
$r_{S1} = r_{S2} = r_{S3} = r_{S4} = r_{\bar{S}1} = r_{\bar{S}2} = r_{\bar{S}3} = r_{\bar{S}4}$	30 $m\Omega$
$r_{Sfc} = r_{Dfc}$	30 $m\Omega$
$r_{C1} = r_{C2}$	30 $m\Omega$
$r_{C3} = r_{CO}$	150 $m\Omega$
$r_{bat1} = r_{bat2}$	10 $m\Omega$
Resistance Line	***Value***
r_{line_bat1}	40 $m\Omega$
r_{line_bat2}	20 $m\Omega$
r_{line_fc}	60 $m\Omega$

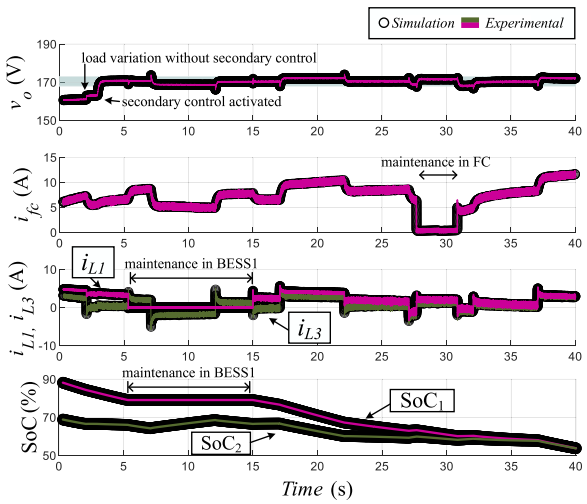

FIGURE 19. MG under load maneuver with initial conditions: SoC$_1$ = 90 % and SoC$_2$ = 70 %. Maintenance is scheduled at 5 s for BESS1 and 27 s for FC. Experimental results are shown as a continuous line, while Simulink simulations are represented by a dashed line with circular markers.

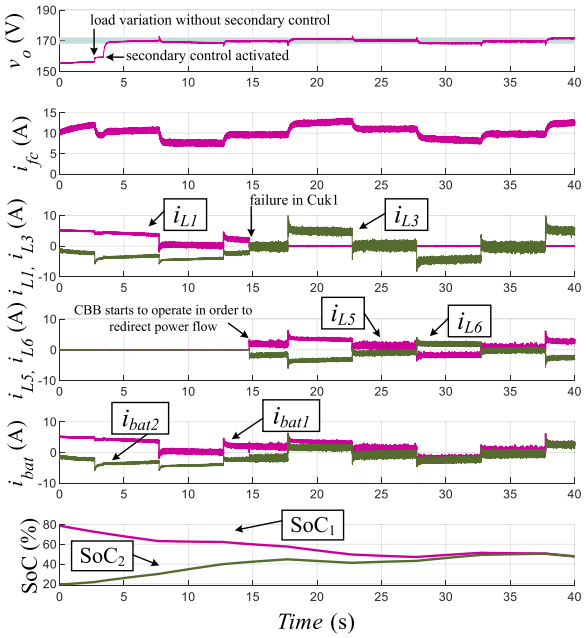

FIGURE 20. MG under load maneuver. Initial SoC$_1$ = 80 % and SoC$_2$ = 20 %, with failure in Cuk1 at 14.5 s.

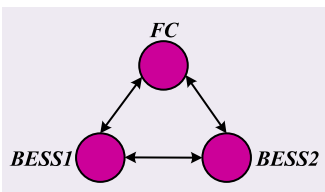

FIGURE 21. Communication architecture between BESS1, BESS2 and FC for the redundancy-based dc MG.

the BESS units also have their capacities reduced to speed up the equalization, which occurs at 33 s. In addition, there are steps of load with $\Delta P_{load} \approx 250$ W, with the transient being absorbed by the BESS units, while the FC has a slow transient during the dc load variation.

At 3 s into the elapsed time, the fuzzy-based secondary voltage control is activated, setting v_o to operate at v_{ref} (170 V). Consequently, during dc load variation and a failure in Cuk1 followed by the power flow redirection, the voltage v_o remains within an interval between 168 V and 172 V. With a voltage deviation of approximately 1.1% for this case, the secondary voltage control has significant performance in the redundancy-based dc MG.

Subsequently, at 14.5 s into the elapsed time, the SoC-sharing function acts to redirect the current from CBC to the auxiliary module (CBB) due to a failure in Cuk1, resulting in $i_{L1} = 0$. As a result, i_{bat1} and i_{bat2} do not experience any issues in their waveform behavior. In addition, if a Cuk1 failure occurs, there is no variation, as i_{bat1} and i_{bat2} remain similar, ensuring that δv_{bat1} and δv_{bat2} are incorporated into the average along with δv_{fc} to determine δv. As a result, the performance on the main dc-link remains stable. In conclusion, the overall efficiency for this experimental result, calculated using (21), is approximately $\eta = 90.1\%$.

C. COMPARISON WITH OTHER METHODOLOGY

This section presents a comparison with a conventional consensus approach utilizing a PI controller. Initially, the multiagent system from [26] is implemented in the redundancy-based dc MG to achieve voltage restoration. Thus, a communication framework utilizing adjacent sources with N nodes is employed, as depicted in Fig. 21, when considering FC and BESS units. As the system determines the observed average dc-link voltage of the ith source (v_{avgi}), whith the redundancy-based dc MG having BESS1, BESS2, and FC as dc sources (from $i = 0$ to 3), the v_{avgi} at time t is defined in (22).

$$v_{avgi}(t) = v_{0i}(t) + \frac{a_v}{|N_i|}\int_0^t \sum_{j\in N_i}(v_{avgj}(\tau) - v_{avgi}(\tau))d\tau \tag{22}$$

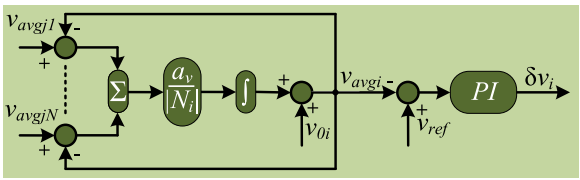

FIGURE 22. Control diagram for the PI-consensus-based approach from [26].

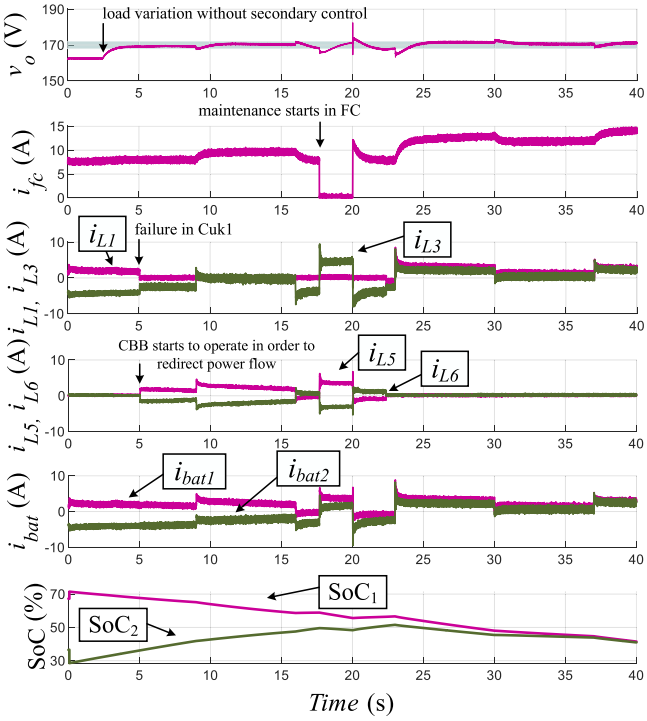

FIGURE 23. Redundancy-based dc MG under load maneuver controlled by the proposed fuzzy-based approach for secondary voltage regulation. The initial conditions are $SoC_1 = 70\,\%$ and $SoC_2 = 30\,\%$. A failure occurs in Cuk1 between 5 s and 22.5 s, while maintenance for FC is scheduled at 17.5 s.

where v_{0i} represents the initial voltage, a_v denotes the consensus gain of the average dc-link, N_i corresponds to the number of adjacent nodes, and v_{avgj} is the state variable of an adjacent node. Subsequently, the contribution δv_i from each dc source (BESS1, BESS2, and FC) can be individually calculated as follows:

$$\delta v_i = k_{pv}(v_{ref} - v_{avgi}(t)) + k_{iv}\int_0^t (v_{ref} - v_{avgi}(\tau))\,d\tau \tag{23}$$

where k_{pv} and k_{iv} represent the proportional and integral gains of the PI controller, respectively, which are utilized to compute δv_i. This adjustment ensures that the dc-link voltage converges to the reference value v_{ref}, as illustrated in Fig. 22.

The proposed strategy is evaluated in comparison with the approach presented in [24], [26], as illustrated in Fig. 23 for the proposed fuzzy-based approach, while Fig. 24 represents the consensus-based technique for voltage restoration. For these experimental results, the initial SoC values for the BESS

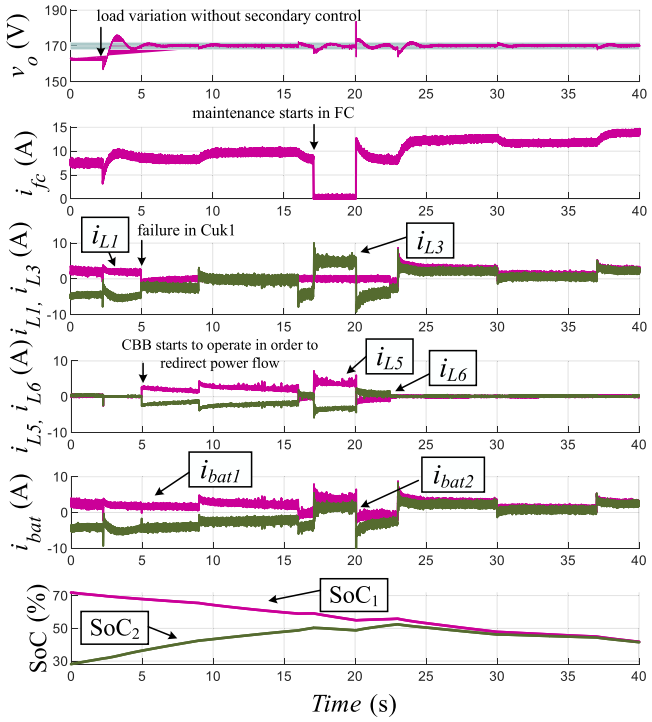

FIGURE 24. Redundancy-based DC MG under load maneuver controlled by a PI-based consensus approach for secondary voltage regulation. The initial conditions are $SoC_1 = 70\,\%$ and $SoC_2 = 30\,\%$. A failure occurs in Cuk1 between 5 s and 22.5 s, while maintenance for FC is scheduled at 17.5 s.

units are set to 70% for SoC_1 and 30% for SoC_2, and there are variations in load demand ($\Delta P_{load} \approx 250$ W). Additionally, during the redundancy-based DC MG operation, a power flow redistribution occurs via the auxiliary module (CBB) between 5 s and 22.5 s.

As observed, both strategies exhibit comparable performance. However, the inclusion of an extra PI controller introduces additional oscillations in the system operating with the consensus-based method, resulting in increased noise in the currents of the redundancy-based dc MG (i_{L5}, i_{L6}, i_{bat1}, and i_{bat2}). Moreover, when designing the PI controller for the consensus-based secondary control, a critical balance must be maintained: If the controller response is too slow, it will fail to converge to the voltage dc-link reference, whereas an excessively fast response may interfere with the primary control of the inductor currents within the redundancy-based dc MG.

When the secondary voltage control is activated, Fig. 24 exhibits an overshoot before reaching steady-state, whereas Fig. 23 presents a more gradual response, with both approaches achieving approximately 91% efficiency. In addition, between 15 s and 25 s of elapsed time, a power flow redirection of CBB occurs due to a failure in Cuk1. Moreover, around 17.5 s, maintenance begins on the FC. Although both strategies achieve SoC equalization among BESS units and voltage restoration of the dc-link, they exhibit distinct behaviors. As noted, Fig. 24 introduces oscillations that may

affect sensitive loads due to the influence of the PI controller, while Fig. 23 maintains a smoother response. Consequently, the fuzzy-based proposed approach proves to be more suitable for improving the performance of the EMS based on a current-source configuration compared to the traditional PI-consensus methodology.

VIII. CONCLUSION

In conclusion, this article introduces a secondary voltage control strategy based on fuzzy logic, designed to maintain the main dc-link voltage at a constant predefined value. The technique is designed in a redundancy-based dc MG, composed of a CBC operating as the main module and a CBB serving as the auxiliary module. Both modules share two common inputs (BESS1 and BESS2). In addition, an FC is connected to the CBC, operating through the droop controller, while the BESS units receive the SoC-sharing function. The complete EMS is responsible for alleviating transients in the FC with a delay in the current response, while the BESS units absorb them with a rapid response.

Moreover, the proposed redundancy-based dc MG, along with the EMS, demonstrates significant reliability in the event of a failure in of the Cuks, with a power flow redirection. The fuzzy-based voltage secondary control improves the main dc-link, resulting in only a 1.1% deviation and ensuring satisfactory performance to increase the resilience of the system. This is achieved alongside the benefit of the redundancy and load compensation provided by the BESS units. Then, this methodology may be suitable for applications in vehicles, aircraft and medical centers that require comprehensive attention to load operation.

First and foremost, the redundancy-based topology is presented. Subsequently, the secondary voltage restoration is introduced, incorporating the droop controller restoration for the FC and the fuzzy-based approach for the BESS units. Later, the stability of the methodology is demonstrated. Finally, the SpeedGoat, operating alongside dSPACE, is responsible for proving and validating the proposed methodology.

As future work, the authors aim to integrate the proposed fuzzy-based approach with the redundancy-based dc MG to accommodate a motor driver as the vehicle load, thereby enhancing the performance of the proposal in [39].

APPENDIX
COMMON COUPLING OF THE REDUNDANCY-BASED DC MG

Defining C_{eq} as the equivalent sum of the output capacitances of all power converters, the term $(-\frac{v_o}{R_o C_{eq}})$ is responsible for eliminating the redundant integration present in both the FC and CBC converters. Consequently, considering a total of n power converters–where, in this case, $n = 2$ since the redundancy-based dc–dc converter is modeled as a single equivalent converter, as shown in Fig. 25–the current i_{Ceq} flowing through the equivalent capacitance C_{eq} is given as follows:

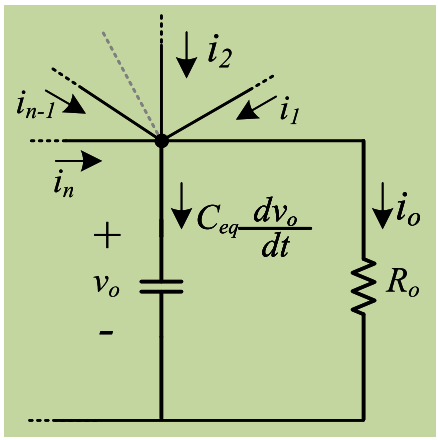

FIGURE 25. Common coupling of a dc-link.

$$\underbrace{i_{Ceq}}_{C_{eq}\frac{dv_o}{dt}} = \underbrace{i_1 - i_o}_{C_{eq}\frac{dv_{o\_1}}{dt}} + \cdots + \underbrace{i_n - i_o}_{C_{eq}\frac{dv_{o\_n}}{dt}} - (n-1)\Big(\underbrace{-\frac{v_o}{R_o}}_{i_o}\Big). \quad (24)$$

REFERENCES

[1] K. D. Hoang and H.-H. Lee, "Accurate power sharing with balanced battery state of charge in distributed DC microgrid," *IEEE Trans. Ind. Electron.*, vol. 66, no. 3, pp. 1883–1893, Mar. 2019, doi: 10.1109/TIE.2018.2838107.

[2] T. A. Fagundes, G. H. F. Fuzato, P. G. B. Ferreira, M. Biczkowski, and R. Q. Machado, "Fuzzy controller for energy management and soc equalization in DC microgrids powered by fuel cell and energy storage units," *IEEE J. Emerg. Sel. Topics Ind. Electron.*, vol. 3, no. 1, pp. 90–100, Jan. 2022, doi: 10.1109/JESTIE.2021.3088419.

[3] S.-Y. Chen and C.-H. Chang, "Optimal power flows control for home energy management with renewable energy and energy storage systems," *IEEE Trans. Energy Convers.*, vol. 38, no. 1, pp. 218–229, Mar. 2023, doi: 10.1109/TEC.2022.3198883.

[4] T. A. Fagundes, G. H. F. Fuzato, C. R. De Aguiar, K. D. A. Ottoboni, M. Biczkowski, and R. Q. Machado, "Management and equalization of energy storage devices for DC microgrids using a soc-sharing function," *IEEE Access*, vol. 8, pp. 78576–78589, 2020, doi: 10.1109/ACCESS.2020.2990191.

[5] A. C. R. and U. B. Manthati, "A hybrid controller assisted voltage regulation and power splitting strategy for battery/supercapacitor system in isolated DC microgrid," *IEEE Trans. Energy Convers.*, vol. 38, no. 3, pp. 1544–1553, Sep. 2023, doi: 10.1109/TEC.2023.3270292.

[6] B. Wang et al., "Consensus-based control of hybrid energy storage system with a cascaded multiport converter in DC microgrids," *IEEE Trans. Sustain. Energy*, vol. 11, no. 4, pp. 2356–2366, Oct. 2020, doi: 10.1109/TSTE.2019.2956054.

[7] D. Xu, A. Xu, C. Yang, and P. Shi, "A novel double-quadrant SoC consistent adaptive droop control in DC microgrids," *IEEE Trans. Circuits Syst. II: Exp. Briefs*, vol. 67, no. 10, pp. 2034–2038, Oct. 2020, doi: 10.1109/TCSII.2019.2945009.

[8] J. Su, K. Li, Y. Li, C. Xing, and J. Yu, "A novel state-of-charge-based droop control for battery energy storage systems to support coordinated operation of DC microgrids," *IEEE Trans. Emerg. Sel. Topics Power Electron.*, vol. 11, no. 1, pp. 312–324, Feb. 2023, doi: 10.1109/JESTPE.2022.3149398.

[9] Y. Mi, J. Guo, Y. Fu, C. Wang, and P. Wang, "Accurate power allocation of multienergy storage island DC microgrid based on virtual power rating," *IEEE Trans. Power Electron.*, vol. 38, no. 1, pp. 261–270, Jan. 2023, doi: 10.1109/TPEL.2022.3201373.

[10] Y. Xia, M. Yu, P. Yang, Y. Peng, and W. Wei, "Generation-storage coordination for islanded DC microgrids dominated by PV generators," *IEEE Trans. Energy Convers.*, vol. 34, no. 1, pp. 130–138, Mar. 2019, doi: 10.1109/TEC.2018.2860247.

[11] T. V. Vu, D. Perkins, F. Diaz, D. Gonsoulin, C. S. Edrington, and T. El-Mezyani, "Robust adaptive droop control for DC microgrids," *Electric Power Syst. Res.*, vol. 146, pp. 95–106, 2017.
[12] T. A. Fagundes et al., "Battery energy storage systems in microgrids: A review of SoC balancing and perspectives," *IEEE Open J. Ind. Electron. Soc.*, vol. 5, pp. 961–992, 2024, doi: 10.1109/OJIES.2024.3455239.
[13] K. Bi, S. Zhang, Y. Zhu, W. Huang, W. Lu, and Q. Fan, "An improved SOC balancing strategy for HVDC modular energy storage system based on low bandwidth communication with enhanced current regulation accuracy," *IEEE Trans. Energy Convers.*, vol. 36, no. 4, pp. 3355–3364, Dec. 2021, doi: 10.1109/TEC.2021.3082300.
[14] L. Xing, F. Guo, X. Liu, C. Wen, Y. Mishra, and Y.-C. Tian, "Voltage restoration and adjustable current sharing for DC microgrid with time delay via distributed secondary control," *IEEE Trans. Sustain. Energy*, vol. 12, no. 2, pp. 1068–1077, Apr. 2021.
[15] D.-H. Dam and H.-H. Lee, "A power distributed control method for proportional load power sharing and bus voltage restoration in a DC microgrid," *IEEE Trans. Ind. Appl.*, vol. 54, no. 4, pp. 3616–3625, Jul./Aug. 2018, doi: 10.1109/TIA.2018.2815661.
[16] X. Lu, J. M. Guerrero, K. Sun, and J. C. Vasquez, "An improved droop control method for DC microgrids based on low bandwidth communication with DC bus voltage restoration and enhanced current sharing accuracy," *IEEE Trans. Power Electron.*, vol. 29, no. 4, pp. 1800–1812, Apr. 2014, doi: 10.1109/TPEL.2013.2266419.
[17] M. S. Alam, F. S. Al-Ismail, F. A. Al-Sulaiman, and M. A. Abido, "Energy management in DC microgrid with an efficient voltage compensation mechanism," *Electric Power Syst. Res.*, vol. 214, 2023, Art. no. 108842, doi: 10.1016/j.epsr.2022.108842. [Online]. Available: https://www.sciencedirect.com/science/article/pii/S0378779622008951
[18] M. S. Alam, F. S. Al-Ismail, and M. A. Abido, "Power management and state of charge restoration of direct current microgrid with improved voltage-shifting controller," *J. Energy Storage*, vol. 44, 2021, Art. no. 103253, doi: 10.1016/j.est.2021.103253. [Online]. Available: https://www.sciencedirect.com/science/article/pii/S2352152X21009476
[19] S. Fang, Y. Xu, H. Wang, C. Shang, and X. Feng, "Robust operation of shipboard microgrids with multiple-battery energy storage system under navigation uncertainties," *IEEE Trans. Veh. Technol.*, vol. 69, no. 10, pp. 10531–10544, Oct. 2020, doi: 10.1109/TVT.2020.3011117.
[20] T. A. Fagundes et al., "A modified redundancy-based energy management system for microgrids: An SoC enhancement approach," *IEEE Trans. Ind. Electron.*, vol. 71, no. 10, pp. 12379–12388, Oct. 2024, doi: 10.1109/TIE.2023.3342325.
[21] M. Jafari, Z. Malekjamshidi, J. Zhu, and M.-H. Khooban, "A novel predictive fuzzy logic-based energy management system for grid-connected and off-grid operation of residential smart microgrids," *IEEE Trans. Emerg. Sel. Topics Power Electron.*, vol. 8, no. 2, pp. 1391–1404, Jun. 2020, doi: 10.1109/JESTPE.2018.2882509.
[22] D. Arcos-Aviles et al., "An energy management system design using fuzzy logic control: Smoothing the grid power profile of a residential electro-thermal microgrid," *IEEE Access*, vol. 9, pp. 25172–25188, 2021, doi: 10.1109/ACCESS.2021.3056454.
[23] H. Ying, *Basic Fuzzy Mathematics for Fuzzy Control and Modeling*, Piscataway, NJ, USA: IEEE, 2000, pp. 1–14.
[24] T. A. Fagundes et al., "Secondary voltage control for DC microgrids: A design perspective for soc with voltage restoration provision," *IEEE Trans. Smart Grid*, vol. 15, no. 6, pp. 5773–5786, Nov. 2024, doi: 10.1109/TSG.2024.3433410.
[25] M. Faisal, M. A. Hannan, P. J. Ker, and M. N. Uddin, "Backtracking search algorithm based fuzzy charging-discharging controller for battery storage system in microgrid applications," *IEEE Access*, vol. 7, pp. 159357–159368, 2019, doi: 10.1109/ACCESS.2019.2951132.
[26] Y. Zeng, Q. Zhang, Y. Liu, X. Zhuang, X. Lv, and H. Wang, "An improved distributed secondary control strategy for battery storage system in DC shipboard microgrid," *IEEE Trans. Ind. Appl.*, vol. 58, no. 3, pp. 4062–4075, May/Jun., 2022, doi: 10.1109/TIA.2022.3153755.
[27] T. Morstyn, A. V. Savkin, B. Hredzak, and V. G. Agelidis, "Multi-agent sliding mode control for state of charge balancing between battery energy storage systems distributed in a DC microgrid," *IEEE Trans. Smart Grid*, vol. 9, no. 5, pp. 4735–4743, Sep. 2018, doi: 10.1109/TSG.2017.2668767.
[28] G. A. H. Pawitan and J.-S. Kim, "MPC-based power management of renewable generation using multi-ESS guaranteeing SoC constraints and balancing," *IEEE Access*, vol. 8, pp. 12897–12906, 2020, doi: 10.1109/ACCESS.2019.2962807.
[29] T. Morstyn, B. Hredzak, R. P. Aguilera, and V. G. Agelidis, "Model predictive control for distributed microgrid battery energy storage systems," *IEEE Trans. Control Syst. Technol.*, vol. 26, no. 3, pp. 1107–1114, May 2018, doi: 10.1109/TCST.2017.2699159.
[30] G. H. F. Fuzato et al., "Droop K-sharing function for energy management of DC microgrids," *IEEE J. Emerg. Sel. Topics Ind. Electron.*, vol. 2, no. 3, pp. 257–266, Jul. 2021, doi: 10.1109/JESTIE.2021.3074889.
[31] T. A. Fagundes, G. H. F. Fuzato, R. F. Q. Magossi, A. L. R. Oliveira, and R. Q. Machado, "A design of a redundancy-based cascaded bidirectional DC–DC converter for improved reliability in energy storage devices," *IEEE Open J. Ind. Electron. Soc.*, vol. 5, pp. 898–915, 2024, doi: 10.1109/OJIES.2024.3446911.
[32] T. Li and L. Parsa, "Design, control, and analysis of a fault-tolerant soft-switching dc–dc converter for high-power high-voltage applications," *IEEE Trans. Power Electron.*, vol. 33, no. 2, pp. 1094–1104, Feb. 2018, doi: 10.1109/TPEL.2017.2684832.
[33] P. Chen, F. Xiao, J. Liu, Z. Zhu, and Q. Ren, "Unbalanced operation principle and fast balancing charging strategy of a cascaded modular multilevel converter–bidirectional DC–DC converter in the shipboard applications," *IEEE Trans. Transport. Electrific.*, vol. 6, no. 3, pp. 1265–1278, Sep. 2020, doi: 10.1109/TTE.2020.3016029.
[34] M. Gleissner and M. M. Bakran, "Design and control of fault-tolerant nonisolated multiphase multilevel DC–DC converters for automotive power systems," *IEEE Trans. Ind. Appl.*, vol. 52, no. 2, pp. 1785–1795, Mar./Apr., 2016, doi: 10.1109/TIA.2015.2497218.
[35] H.-T. Yang, H.-W. Chiang, and C.-Y. Chen, "Implementation of bridgeless Cuk power factor corrector with positive output voltage," *IEEE Trans. Ind. Appl.*, vol. 51, no. 4, pp. 3325–3333, Jul./Aug., 2015, doi: 10.1109/TIA.2015.2409253.
[36] Y. M. Ameen, H. Al-Badrani, and M. N. Abdul Kadi, "Design and simulation of a high-power double-output isolated Cuk converter," *Eastern-Eur. J. Enterprise Technol.*, vol. 5, no. 5, 2021, Art. no. 113.
[37] A. Sadollah, "Introductory chapter which membership function is appropriate in fuzzy system?," in *Fuzzy Logic Based in Optimization Methods and Control Systems and Its Applications*, A. Sadollah, Ed., ch. 1. Rijeka: IntechOpen, 2018.
[38] V. Olunloyo, A. Ajofoyinbo, and O. Ibidapo-Obe, "On development of fuzzy controller: The case of gaussian and triangular membership functions," *J. Signal Inf. Process.*, vol. 2, pp. 257–265, Jan. 2011, doi: 10.4236/jsip.2011.24036cite26.
[39] M. V. R. Campos, L. J. R. Silva, T. A. Fagundes, R. V. A. Neves, V. A. Oliveira, and R. Q. Machado, "Energy management system based on S-shaped functions for series hybrid vehicle under a fully active topology," *IEEE Trans. Veh. Technol.*, vol. 74, no. 3, pp. 4087–4102, Mar. 2025, doi: 10.1109/TVT.2024.3498703.

THALES AUGUSTO FAGUNDES was born in Jundiaí, Brazil. He received the B.S. degree in electrical engineering in 2017, and the M.S. and Ph.D. degrees in electrical engineering with a focus on dynamic systems from the University of São Paulo, São Carlos, Brazil, in 2020 and 2025, respectively.

In 2014, he studied abroad with the University of New South Wales, Sydney, Australia, focusing on courses related to alternative energy sources. From 2022 to 2023, he was a Visiting Researcher with Aalborg University, Aalborg, Denmark. He is currently a Postdoctoral Researcher with the University of São Paulo. His main research interests include microgrids, energy management, and dc–dc converters for renewable energy sources and storage systems.

RAPHAEL SAUER DE CASTRO received the B.Sc. degree in computer engineering from the Federal University of Technology–Paraná (UTFPR), Guarapuava, Brazil, in 2021. He is currently working toward the Ph.D. degree in electrical engineering with the São Carlos School of Engineering, University of São Paulo (EESC/USP), São Carlos, Brazil, with a focus on dynamic systems.

His research interests include dc–dc converters, energy generation, microgrids, system optimization, dynamic systems, and neural networks.

MÁRCIO VON RONDOW CAMPOS was born in Caratinga, Brazil. He received the B.S degree in electrical engineering from the Federal University of Viçosa, Vicosa, Brazil, in 2022, and the M.S. degree in power electronics, in 2024, from the University of Sao Paulo, São Carlos, Brazil, where he is currently working with the Ph.D. degree in electrical engineering.

His main research interests include dc–dc converters for renewable energy sources, microgrids, energy management, and hybrid electric vehicles.

BRUNO MENEGHEL ZILLI was born in Medianeira, Brazil. He received the B.S. degree in electronic engineering from the Federal University of Technology—Paraná, Guarapuava, Brazil, in 2015, the M.S. degree in energy in agriculture engineering from the Western Paraná State University, Cascavel, Brazil, in 2018, and the Ph.D. degree in electrical engineering from the University of São Paulo, São Carlos, Brazil, in 2024.

He is currently a Professor with the Federal University of Technology—Paraná. His main research interests include microgrids, harmonic compensation, energy management, and dc/ac converters for renewable energy sources.

LUCAS JONYS RIBEIRO SILVA (Graduate Student Member, IEEE) was born in Viçosa, Brazil, in 1997. He received the B.S. degree in electrical engineering in 2020 from The Federal University of Viçosa, Vicosa, and the M.S. degree in power electronics and control systems in 2022, from the University of Sao Paulo, São Carlos, Brazil, where he is currently working on the Ph.D. degree in electrical engineering with the University of Sao Paulo.

His main research interests include microgrids, electric and hybrid vehicles, energy management, and dc–dc converters for renewable energy sources and storage systems.

JOSEP M. GUERRERO (Fellow, IEEE) received the B.S. degree in telecommunications engineering, the M.S. degree in electronics engineering, and the Ph.D. degree in power electronics from the Technical University of Catalonia, Barcelona, in 1997, 2000, and 2003, respectively.

In 2019, he was a Villum Investigator with the Villum Fonden, which supports the Center for Research on Microgrids (CROM), Aalborg University, Aalborg, Denmark. Since 2011, he has been a Full Professor with the Department of Energy Technology, Aalborg University. His research interests include different microgrid aspects, including applications as remote communities, energy prosumers, and maritime and space microgrids.

RICARDO QUADROS MACHADO (Senior Member, IEEE) was born in Santa Maria, Brazil. He received the B.S. degree from the University of Santa Maria, Santa Maria, Brazil, in 1997, the M.S. degree and the Ph.D. degrees in electrical engineering from the University of Campinas, Campinas, Brazil, in 2000 and 2005, respectively.

From 2002 to 2003, he was a Visiting Researcher with the University of Padova, Padova, Italy, and from 2005 to 2007, he was a postdoctorate with the Federal University of Santa Maria, Santa Maria, Brazil. From 2013 to 2014, he was Visiting Professor with the University of Toronto, Toronto, Canada. From 2007 to 2018, he was Assistant Professor with the University of Sao Paulo, Sao Carlos, Brazil. He is currently an Associated Professor with the University of Sao Paulo. His main research interests include processing of energy in dc–dc and dc/ac converters, digital control of power converters, distributed generation systems, smart grids, and control of renewable energy sources.

Open Access provided by 'Coordenação de Aperfeiçoamento de Pessoal de Nível Superior (CAPES) - ROR identifier: 00x0ma614' within the CRUI CARE Agreement